applied sciences

MDPI

Article

Jaw Crusher Frame Material Selection: Strength, Resonance Margin, Fatigue and Heating of Grey Cast Iron, Polymer Concrete and FDM-Printed ABS

Ainur Kadirsizova [1], Dinara Baskanbayeva [1,*], Jasur Safarov [2], Darkhan Yerezhep [1,3,*] and Kassym Yelemessov [1]

[1] Institute of Power Engineering and Mechanical Engineering Named After A. Burkitbaev, Satbayev University, Almaty 040714, Kazakhstan; a.kadirsizova@satbayev.university (A.K.); k.yelemessov@satbayev.university (K.Y.)
[2] Faculty of Mechanical Engineering, Tashkent State Technical University, Tashkent 100095, Uzbekistan; jasursafarov@yahoo.com
[3] Department of Science and Commercialization, Almaty Management University, Rozybakiyev Str., 227, Almaty 050060, Kazakhstan
* Correspondence: d.baskanbayeva@satbayev.university (D.B.); darhan_13@physics.kz (D.Y.)

Featured Application

The admissible-force chart and the critical heat flux introduced here give designers of small and medium jaw crushers a quick and measurable way to identify the failure mechanism that limits a candidate frame material before detailed design begins.

Abstract

The frame of a jaw crusher is subjected to cyclic crushing loads, bearing reactions and localised heating, making material selection dependent on multiple interacting failure mechanisms. This study presents a comparative computational assessment of grey cast iron (GCI), epoxy polymer concrete (PC) and fused deposition modelling (FDM)-printed acrylonitrile butadiene styrene (ABS) for a common jaw crusher frame geometry with a 150 × 250 mm feed opening and an operating speed of 300 rpm. Static, modal and steady-state thermal finite-element analyses were combined with analytical models of load spectra, forced vibration, fatigue, transient heating and feasibility-constrained multi-criteria decision-making. At crushing forces of 50 and 150 kN, the calculated peak von Mises stresses ranged from 18.1 to 21.3 MPa and from 54.1 to 64.0 MPa, respectively. Under the adopted static and fatigue safety requirements of 3.0 and 1.5 and a simplified load introduction, the estimated fatigue-governed admissible crushing forces were approximately 110 kN for GCI (95 kN for the most unfavourable biaxial stress state) and at most 41 kN for ABS; the ABS value is an upper bound that falls to 6–23 kN with strengths measured on printed specimens. The original PC geometry was limited to approximately 7–8 kN by tensile strength. The GCI and PC values are estimates based on assumed principal stresses. Thus, the original GCI configuration satisfies the adopted structural criteria at 50 kN but not the fatigue requirement at 150 kN. A similarity-law check exposed an input error in the original PC and ABS modal analyses; the frequencies consistent with the specified properties, predicted analytically from the GCI solution, are 885 and 363 Hz, respectively, compared with 958 Hz for GCI. Preliminary plate-theory estimates suggest that a PC frame with walls thickened by 2.5–2.7-fold could meet the static requirement at 50 kN with 13–19% lower mass than GCI; however, its fatigue margin lies within the uncertainty of the fatigue model, and its estimated hot-spot temperature (≈112–115 °C) exceeds the binder limit. These estimates have not been verified by finite-element analysis. The study demonstrates that material-specific strength criteria, fatigue resistance and thermal limitations must be evaluated before

Check for updates

Received: 26 October 2026
Revised: 25 November 2026
Accepted: 26 November 2026
Published: 28 November 2026

Copyright: © 2026 by the authors. Licensee MDPI, Basel, Switzerland. This article is an open access article distributed under the terms and conditions of the Creative Commons Attribution (CC BY) license.

compensatory multi-criteria ranking. The resulting framework provides a comparative screening tool rather than experimentally validated absolute design limits.

Keywords: jaw crusher; machine frame; eccentric shaft; finite-element analysis; grey cast iron; polymer concrete; FDM-ABS; high-cycle fatigue; resonance margin; TOPSIS

1. Introduction

Jaw crushers remain the workhorse of primary crushing in mining, quarrying and the production of construction aggregates [1]. Their process side is well understood. Fundamental models link the kinematics of the swing jaw with rock breakage and the capacity of industrial machines [2]; energy analyses quantify the share of the supplied power that is spent on fracture itself [3]; regression and neuro-fuzzy models predict energy consumption from operating data [4]. Calibrated discrete element method (DEM) simulations reproduce throughput, power draw and jaw forces as functions of the closed-side setting and stroke frequency [5], and DEM coupled with multibody dynamics now resolves the drivetrain loads of large crushers under normal and choked conditions [6]. Kinematic models of the jaw crusher drive mechanism continue to be refined [7,8], and finite-element analysis (FEA) has been applied mainly to the crushing components, for example, to optimise the swing jaw [9]. The forces generated in the crushing chamber are therefore well described; how they travel into the load-bearing structure is followed far less often.

That structure is the frame. In a single-toggle jaw crusher, the frame carries the eccentric shaft in two bearings, takes the crushing force through the bearing housings and the toggle seat, and transmits a periodic load to the foundation. When it is underdesigned, the consequences are costly: Rusiński et al. [10] documented fast-growing fatigue cracks and bolt failures in the supporting structure of a jaw crusher after a short period of operation and investigated them with combined measurements and numerical analysis. DEM-based load histories have recently been combined with fatigue damage accumulation to estimate the service life of crusher components [11]. Seen as the support of a rotating machine, the frame has to meet three requirements. Its natural frequencies must stay clear of the shaft speed and its harmonics; the cyclic load must not accumulate fatigue damage; and the bearing seats must remain within the temperature limits of the frame material. Grey cast iron meets these requirements through a combination of stiffness, compressive strength, castability and internal damping, and it remains the traditional material of machine beds and frames [1,12]. Its fatigue failure, however, is controlled by tensile cracking [13], so criteria developed for ductile metals cannot be transferred to it directly; brittle materials require dedicated static and fatigue criteria [14].

Machine-tool engineering offers a well-studied alternative. Polymer concrete, also known as mineral casting, has replaced cast iron in many machine-tool beds because it combines adequate stiffness with high damping and low thermal conductivity [12]. Its damping has been characterised experimentally [15], a lathe with a polymer concrete bed has been tested in hard turning [16], and recent work raises damping further through periodic meta-structures [17] and optimised aggregate gradation [18]. Steel-reinforced epoxy granite raised the natural frequencies of a vertical machining centre base by more than 50% relative to cast iron [19]. The same material, however, conducts heat poorly: in a lathe with a steel-reinforced epoxy granite bed, heat from the feed drive accumulated in the embedded steel guideways, and the thermal error was 1.7–1.8 times that of the cast-iron machine [20]. Polymer concrete typically reaches 70–120 MPa in compression [21], but its tensile strength is about an order of magnitude lower, and the binder limits the service temperature: heating markedly changes the fracture behaviour of epoxy polymer

concrete [22]. Its fatigue behaviour under tension-dominated loading is documented far less than that of cement concrete; bending fatigue tests on epoxy- and polyurethane-based mixes at stress levels of 0.2–0.5 of the static strength followed power-law S–N relations [23]. In a machine tool, these limitations are secondary. In a crusher, they become primary: the frame carries loads one to two orders of magnitude larger than typical cutting forces, is loaded in tension near the bearing supports and is heated by bearing friction.

Additive manufacturing adds a third, and the cheapest, option. Fused deposition modelling (FDM) of acrylonitrile butadiene styrene (ABS) produces a frame directly from the CAD model, which is attractive for teaching rigs and functional prototypes. FDM-ABS is strongly anisotropic, with strength governed by raster orientation and interlayer bonding [24,25]. Its fatigue life depends on print parameters such as infill pattern and nozzle diameter [25,26], and these parameters affect fatigue differently from static strength [27]. Fatigue life also drops sharply when the ambient temperature rises from 50 to 70 °C [28]. A printed frame therefore cannot be judged by static strength alone; fatigue and temperature matter at least as much.

Choosing among such different materials involves conflicting criteria: strength, fatigue margin, stiffness, temperature limit and mass. Multi-criteria decision-making (MCDM) methods, including the Technique for Order of Preference by Similarity to Ideal Solution (TOPSIS) [29], are widely used for material selection, yet the ranking depends on the normalisation and weighting scheme [30,31]. Stochastic multi-criteria acceptability analysis addresses weight uncertainty by exploring the weight space and describing how often each alternative attains each rank [32]. A further difficulty is that TOPSIS is compensatory: a large advantage in mass can offset an unacceptable safety factor. Hard engineering constraints therefore have to be checked separately, before the ranking.

To the authors' knowledge, a jaw crusher frame has not yet been compared for cast iron, polymer concrete and an additively manufactured polymer within one framework covering static strength, resonance margin, fatigue and heating. This study asks which material is admissible for crushing soft and hard rock and which failure mechanism limits each alternative. Its contributions are as follows:

- For a load-bearing frame of fixed geometry, the stress state under a given load introduction is shown to be practically material-invariant. This turns two finite-element load cases into a matrix of admissible crushing forces by static, fatigue and thermal criteria, which identifies the governing failure mechanism of each material.
- Finite-element results are combined with analytical models of the eccentric-drive load spectrum, forced vibration, fatigue and transient heating, so that steady-state fields translate into admissible loads, service life and time to the thermal limit.
- A similarity-law check for comparative finite-element studies (stress invariance, frequency scaling with $\sqrt{(E/\rho)}$, invariance of mode-frequency ratios) is proposed; applied to the present data, it exposed an input error in the modal results for the lightweight materials and predicted the frequencies consistent with the specified properties analytically from the GCI solution.
- A material-adapted polymer concrete frame is assessed preliminarily by plate scaling, which indicates that the wall thickening required to remove the tensile deficit raises the hot-spot temperature beyond the binder limit.
- The robustness of the conclusions is tested against uncertain parameters (fatigue reduction factor, mean-stress criterion, polymer concrete strength and S–N slope, printed-ABS strength, heat flux, variants of the decision matrix) and against the choice of weights (2×10^5 Monte Carlo weight vectors); the influence of the load introduction is discussed but not computed.

The framework is aimed at one design decision: whether a candidate material can carry the crushing loads of a given frame and, if not, which failure mechanism must be addressed. Because the stress field of a fixed geometry hardly depends on the material, two FE load cases are converted once into an admissible-force chart (as described in Section 3.6) in which every criterion is expressed in the same quantity, the crushing force. The chart shows the governing mechanism of each material and its margin to the required load, and thus whether a stronger grade, local reinforcement or thicker sections can close the gap, or whether the material should be rejected. The thermal limit is expressed as a critical heat flux that can be compared with a value measured on an operating machine, and admissibility constraints are applied before the compensatory ranking, so that a light but inadmissible material cannot win on mass. Multi-criteria ranking thus becomes the last step of the screening rather than its basis.

The study is computational, and its conclusions are comparative; Section 4.6 outlines the experiments needed to turn them into absolute design values.

2. Materials and Methods

2.1. Object of Study

A parametric solid model of a single-toggle jaw crusher frame was built in SolidWorks 2023 (Dassault Systèmes, Vélizy-Villacoublay, France) (Figure 1). The frame is designed for an eccentric shaft of 60 mm diameter and a feed opening of 150 × 250 mm, which corresponds to crushers of small and medium capacity with 5–11 kW drives. The shaft speed is $n = 300$ rpm ($f_{op} = 5$ Hz). The model comprises the side walls, five horizontal stiffening ribs on the front wall, two bearing supports and four mounting feet; the characteristic wall thickness is $\delta = 25$ mm. The frame volume taken from the model is $V \approx 7.8 \times 10^{-3}$ m^3, and frame masses were computed as $m = \rho V$. The same geometry, mesh and boundary conditions were used for all three materials. This design deliberately excludes geometry optimisation for each material and isolates the effect of material properties; its consequences are discussed in Section 4.1.

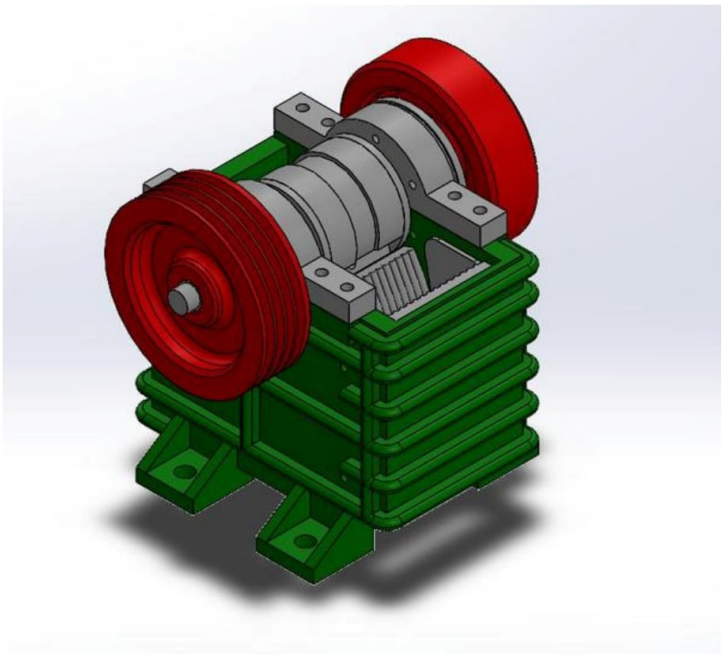


Figure 1. Solid model of the single-toggle jaw crusher: frame (green), eccentric shaft with bearing housings, swing jaw and flywheels (red).

2.2. Materials

Material properties and their sources are listed in Table 1. All three materials were modelled as linear elastic and isotropic. For grey cast iron (GCI; strength class roughly corresponding to EN-GJL-200 [33]), this is an approximation: grey iron has no yield point, and the 200 MPa used here is its minimum ultimate tensile strength in separately cast test pieces [33]. For FDM-ABS, the isotropic elastic model is supported by tensile tests with digital image correlation, in which raster and build orientation had a negligible effect on the Young's modulus and Poisson's ratio of printed ABS [34]. The strength, in contrast, is strongly anisotropic and is governed by raster orientation and interlayer bonding [24,25]. The tensile strength of 55 MPa adopted here exceeds all values measured on printed specimens: about 8 MPa for transverse and 23 MPa for on-axis rasters of ABS P400 [35], and 27.5–30.8 MPa for a current production grade printed upright or on edge [36]. All strength-based ABS results are therefore optimistic upper bounds; they are flagged as such in Section 3.1, Section 3.5, and Section 3.6 , and Appendix B (Table A2) repeats the assessment with the measured strengths. For epoxy polymer concrete (PC), a design strength of 80 MPa was adopted for a compressive strength of 100 MPa (partial material factor 1.25); both values lie within the 70–120 MPa range reported for polymer concretes [21]. The tensile strength of PC, 10 MPa, is the upper value reported for mineral castings, whose compressive strength is about nine times the tensile strength [37]; the effect of a higher value is examined in Section 3.1.

Table 1. Design material properties (input data of the finite-element model).

Property	GCI	PC	FDM-ABS
Young's modulus E, GPa	110 [20,33]	30 [20]	2.3 [34,36]
Poisson's ratio ν	0.26 [33]	0.22 [3]	0.36 [34]
Density ρ, kg/m^3	7200 [20,33]	2300 [20]	1050 [36,38]
Tensile strength σ_t, MPa	200 [33]	10 [37]	55 [4]
Compressive strength σ_c, MPa	700 [33]	100 [20,21]	55 [5]
Strength used in $n_{s,VM}$, σ_{lim}, MPa	200 (σ_t)	80 ($0.8\sigma_c$)	55 (σ_t)
Thermal conductivity λ, W/(m·K)	50 [20,33]	1.0 [20]	0.17 [38]
Specific heat c, J/(kg·K)	460 [20,33]	1000 [37]	1400 [38]
Thermal expansion coefficient α, 10^{-6} K^{-1}	10.5 [33]	12 [20,37]	90 [38]
Service-temperature limit T_{lim}, °C	—(not limiting)	80 (cold-cured)/100 (hot-cured) [1]	80–100 [2]
Frame mass $m = \rho V$, kg	56.2	17.9	8.2
Specific stiffness $\sqrt{(E/\rho)}$, m/s	3909	3612	1480

[1] Design assumption; the actual limit depends on the glass transition temperature of the binder. [2] Design assumption based on the heat deflection temperature of ABS grades (100 °C at 1.82 MPa for a printed production grade [36]); the lower value allows for the sharp drop in fatigue life of printed ABS between 50 and 70 °C [28]. [3] 0.25 in [20]; Poisson's ratio affects the results only weakly (Section 3.1). [4] Optimistic upper bound: measured strengths of printed ABS are 8.4–23.1 MPa for ABS P400, depending on raster orientation [35], and 27.5–30.8 MPa (yield) for ABS-M30 printed upright or on edge [36]; see Table A2. [5] Not used: ABS is assessed with the von Mises criterion and σ_t.

All values refer to room temperature and quasi-static short-term loading: for GCI, to separately cast test pieces of EN-GJL-200 [33]; for PC, to fully cured mineral castings; for ABS, to printed parts tested in the stated orientation. At the temperatures computed for the GCI frame (≤56 °C), temperature effects on its properties are negligible. The values for PC and ABS hold only below the service limits T_{lim}: the fracture behaviour of epoxy PC changes markedly on heating [22], and the fatigue life of printed ABS drops sharply between 50 and 70 °C [28]. This is why T_{lim} enters the feasibility filter (Section 2.12).

2.3. Loads and Boundary Conditions

The frame was fixed at the bolt holes of the mounting feet (fixed geometry: zero displacements in all three directions), which idealises the bolted foundation joint as rigid.

Three loads were applied: (i) a distributed load of 5 kN on the bearing seats (Bearing Load); (ii) a distributed crushing force F_{cr} of 50 or 150 kN on the inner side faces, representing the jaw reaction; and (iii) self-weight ($g = 9.81$ m/s^2). The crushing force was estimated from the compressive strength of the rock and the projected contact area:

$$F_{cr} = \sigma_{c,rock} A_c = 150 \text{ MPa} \times (0.02 \times 0.05) \text{ m}^2 = 150 \text{ kN} \quad (1)$$

For limestone ($\sigma_c \approx 50$ MPa), the same area gives 50 kN. The contact area $A_c = 20 \times 50$ mm is an assumption not tied to a particular feed size; Section 3.6 therefore converts the results into admissible forces that do not depend on this choice.

In an operating single-toggle jaw crusher, the crushing force is transmitted through the swing jaw, eccentric-shaft bearings, toggle mechanism and corresponding frame supports. The simplified loading scheme adopted in this study does not fully reproduce this three-dimensional force-transfer mechanism or the associated contact and joint effects. It was selected to provide identical nominal loading conditions for the three candidate materials and thereby isolate the influence of material properties within a common computational configuration. Consequently, the calculated stress concentrations, safety factors and admissible crushing forces must be interpreted as conditional results for the prescribed load path rather than validated operating limits for an industrial crusher. Although the comparative trends provide useful preliminary evidence, their transfer to a real machine requires verification using a load model incorporating bearing reactions, toggle-seat forces and mounting-joint compliance. The present analysis therefore serves as a material-screening assessment and does not replace a complete structural verification of the crusher assembly.

The forces at the frame supports follow from the equilibrium of the swing jaw. Neglecting inertia, friction and the small inclination of the toggle plate, the resultant crushing force F_{cr}, acting at a distance a below the eccentric axis, is balanced by the reaction of the eccentric shaft, $R_e = F_{cr}(1 - a/L)$, and by the toggle force $R_t = F_{cr} \cdot a/L$, where L is the distance from the eccentric axis to the toggle contact. For a resultant at mid-height of the jaw ($a/L = 0.5$), each of the two bearings would carry $F_{cr}/4$ and the toggle seat $F_{cr}/2$. The frame thus receives F_{cr} on the fixed-jaw seat of the front wall and the opposite forces R_e and R_t at the bearing seats and the toggle seat; in operation, the crushing force is self-equilibrated within the frame, and the foundation carries only weight and inertia forces. The simplified scheme of this study transmits F_{cr} to the foundation instead. The two schemes load the frame differently. Replacing one by the other therefore changes not only the level of the stresses but also their distribution: the critical locations may move, for example, from the mounting feet towards the bearing and toggle seats, and the principal-stress ratios at them may change. Stress invariance (Section 2.6) holds within each scheme, because, for given forces and fixtures, the stress field hardly depends on the material; under the real load introduction, the three frames would therefore again share practically one stress field, but that field cannot be inferred from the present one. All the results of this study refer to the adopted scheme. Section 3.1 states which conclusions depend on the load introduction; an analysis with the real load introduction was not part of this study.

2.4. Finite-Element Model

The analyses were performed in SolidWorks Simulation 2022, SP3.0 (version 30.3, Dassault Systèmes SolidWorks Corporation, Waltham, MA, USA) with quadratic ten-node tetrahedral elements. The global element size was 8 mm, refined locally to 4 mm in stress-concentration zones (bearing bores, rib fillets, mounting feet). Halving the element size changed the maximum von Mises stress by less than 3.5%. Convergence is meaningful only for stresses away from the singular points at the edges of the fixed faces; the peaks reported here lie in the fillets and gussets of the mounting feet and at the bearing supports (Figure 2), i.e., outside such points.

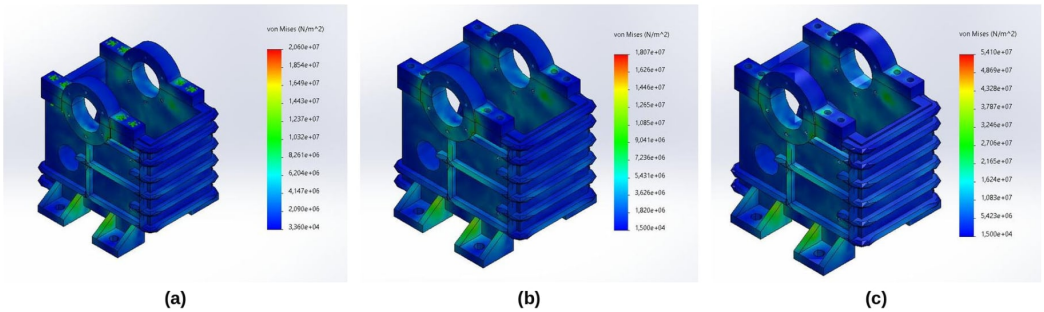


Figure 2. Von Mises stress fields (legend in N/m^2, decimal comma in the software output): (**a**) GCI frame at 50 kN; (**b**) FDM-ABS frame at 50 kN; (**c**) FDM-ABS frame at 150 kN ($n_{s,VM} = 1.02$, upper bound). The reported peaks lie in the fillets and gussets of the mounting feet, outside the singular points at the edges of the fixed faces (Section 2.4).

2.5. Static Strength Criteria

The von Mises safety factor serves as a common comparative measure:

$$n_{s,VM} = \frac{\sigma_{lim}}{\sigma_{VM,max}} \tag{2}$$

For ductile ABS, criterion (2) is physically appropriate. For the other two materials, it is only a comparative index and is complemented by criteria for brittle media. For GCI, whose failure is controlled by tension [13], the brittle Coulomb–Mohr criterion is used [14]:

$$\frac{1}{n_{s,MC}} = \frac{\sigma_1}{\sigma_t} - \frac{\sigma_3}{\sigma_c}, \qquad \sigma_1 \geq 0 \geq \sigma_3 \tag{3}$$

For PC, the decisive check is the maximum principal tensile stress:

$$n_{s,t} = \frac{\sigma_t}{\sigma_{1,max}} \tag{4}$$

The principal stresses in the peak zone were estimated from its stress state. The maximum is located in the gussets of the mounting feet, which work in bending; on the tensile surface of such a zone, the stress state is close to uniaxial, so $\sigma_1 \approx \sigma_{VM}$ and $\sigma_3 \approx 0$ were adopted as the base case. Since the principal stresses at the critical point were not evaluated separately, the influence of biaxiality is bounded rather than computed. For plane stress at a free surface, $\sigma_1 \leq (2/\sqrt{3})\sigma_{VM} = 1.155\sigma_{VM}$, the maximum being reached for $\sigma_2 = \sigma_1/2$. A compressive second principal stress lowers σ_1 below σ_{VM}; for the strength ratio $\sigma_t/\sigma_c = 0.29$ of GCI, such a state is less critical for criterion (3) than $\sigma_1 = 1.155\sigma_{VM}$ with $\sigma_3 = 0$, which is therefore the most unfavourable case for all brittle-material criteria and for the fatigue check of GCI and of the tension zones of PC. Results are reported for the base case, with this upper bound given alongside (Table 2, Section 3.1 and Appendix B, Table A5). The principal stresses were not extracted from the finite-element solution. All quantities that depend on them—the Coulomb–Mohr safety factor of GCI, the principal-tensile-stress safety factor of PC, the fatigue factors of GCI and of the tension zones of PC, and the admissible forces and rankings derived from them—are therefore estimates for these assumed stress states rather than principal-stress-based safety factors verified by the FE analysis; only the von Mises-based quantities are taken directly from it. For GCI, criterion (3) with $\sigma_3 \approx 0$ gives $n_{s,MC} = \sigma_t/\sigma_1$; the compressed side of the gusset is not critical given $\sigma_c = 700$ MPa. The required static safety factor was set to $n_{s,req} = 3.0$ as a design value for a cast structure under impact-type loading.

Table 2. Peak von Mises stresses (FEA) and static safety factors; values based on σ_1 are estimates for assumed stress states (Section 2.5).

Quantity	GCI	PC	FDM-ABS
$\sigma_{VM,max}$ at 50 kN, MPa	20.6	21.31	18.07
$\sigma_{VM,max}$ at 150 kN, MPa	63.8	64.0	54.1
Ratio $\sigma(150\ kN)/\sigma(50\ kN)$ (3.00 if linear)	3.10	3.00	2.99
σ_{lim}, MPa	200	80	55
$n_{s,VM}$ at 50/150 kN	9.71/3.13	3.75/1.25	3.04/1.02 [a]
σ_1 in the peak zone at 50/150 kN, assumed ($\sigma_1 \approx \sigma_{VM}$; in brackets: upper bound $\sigma_1 = 1.155\sigma_{VM}$), MPa	20.6/63.8 (23.8/73.7)	21.3/64.0 (24.6/73.9)	—
$n_{s,MC}$ (GCI) or $n_{s,t}$ (PC) at 50/150 kN, estimates for the assumed σ_1	9.71/3.13 (8.41/2.71)	0.47/0.16 (0.41/0.14)	—
Self-weight of the frame, kN (% of 50 kN)	0.55 (1.1%)	0.18 (0.35%)	0.08 (0.16%)

[a] Upper bound: isotropic properties of the most favourable raster orientation (Section 2.2); values for measured strengths of printed ABS are given in Table A2.

2.6. Modal Analysis and Similarity-Law Check

The first five natural frequencies were obtained from the generalised eigenvalue problem with the same fixtures:

$$([K] - \omega_i^2[M])\{\varphi_i\} = \{0\}, \qquad f_i = \frac{\omega_i}{2\pi}, \qquad k_r = \frac{f_1}{f_{op}} \tag{5}$$

where k_r is the resonance margin, and $f_{op} = n/60 = 5$ Hz. If geometry and fixtures are identical, and the whole model is made of one material, the stiffness matrix is proportional to E (with a weak dependence on ν), and the mass matrix is proportional to ρ. Two testable consequences follow: all frequencies scale by the same factor, and the ratios f_i/f_1 do not depend on the material:

$$\frac{f_i^{(m)}}{f_i^{(GCI)}} = \sqrt{\frac{E_m/\rho_m}{E_{GCI}/\rho_{GCI}}}, \qquad \frac{f_i^{(m)}}{f_1^{(m)}} = \text{const}(m) \tag{6}$$

Inverting (6) gives the effective modulus actually used by the model:

$$E_{eff}^{(m)} = E_{GCI}\left(\frac{f_1^{(m)}}{f_1^{(GCI)}}\right)^2 \frac{\rho_m}{\rho_{GCI}} \tag{7}$$

Likewise, for mass-normalised mode shapes, the maximum amplitude is proportional to $1/\sqrt{\rho}$, which independently checks the density used in the analysis. The same principle applies to statics: in a linear elastic problem with prescribed forces and rigid fixtures, the stress field does not depend on E and depends only weakly on ν [39], and stresses grow linearly with the load. A violation of any of these consequences points to an input error or to bodies of an assembly that were not reassigned to the new material. Relation (6) is exact for the discretised problem: with identical geometry, mesh and fixtures, the stiffness matrix scales with E when ν is equal and the mass matrix scales with ρ, so every eigenfrequency of the reference solution changes by the same factor, and the mode shapes remain unchanged. Only a difference in Poisson's ratio breaks this scaling. For plate-like walls, its effect can be estimated from the bending stiffness, proportional to $E/(1-\nu^2)$, and from the shear stiffness, proportional to $E/(1+\nu)$: relative to (6), the frequencies change by −1.0% and

+1.6%, respectively, for PC and by +3.5% and −3.7% for ABS. These plate relations are a simplified estimate that does not represent the three-dimensional behaviour of the frame; frequencies obtained from (6) are therefore reported as analytical predictions and are distinguished from FE results throughout.

2.7. Steady-State Thermal Analysis and Critical Heat Flux

The steady heat conduction equation $\nabla\cdot(\lambda\nabla T) = 0$ was solved. A heat flux, $q = 1000$ W/m^2, was prescribed on the inner wall faces in contact with the jaws. This value is a design assumption, and its uncertainty is handled through the critical heat flux introduced below. Its order of magnitude follows from the energy balance of the machine. Comminution typically uses less than 10% of the input energy to create new surface [3]; the rest is ultimately dissipated as heat, and the no-load power of jaw crushers alone amounts to 40–50% of the rated power [40]. With the heated chamber-wall area of 0.15–0.18 m^2 estimated below, $q = 1000$ W/m^2 corresponds to 150–180 W, i.e., to 1.4–3.6% of the installed drive power of 5–11 kW entering the frame through the chamber walls. Because this share has not been measured, the thermal results are also reported for $q = 300$–3000 W/m^2 (Appendix B, Table A3), a decade that corresponds to 0.4–11% of the installed power. Convection with $h = 12$ W/(m^2·K) and $T_\infty = 25$ °C was applied to all outer faces. The heat generated in one bearing unit was estimated as

$$P_b = \mu F_b v, \qquad v = \frac{\pi d n}{60} = 0.942 \text{ m/s}, \qquad P_b = 0.005 \cdot 5000 \cdot 0.942 \approx 23.6 \text{ W} \tag{8}$$

where $\mu = 0.005$ is a deliberately high value of the load-independent friction coefficient of a rolling bearing, $d = 60$ mm is the shaft diameter and $F_b = 5$ kN is the bearing reaction. In the model, this heat was applied as a uniform flux $q_b \approx 500$ W/m^2 on the bearing-unit surfaces, which, at $P_b = 23.6$ W, corresponds to a heat-transfer area $A_b = P_b/q_b \approx 0.047$ m^2. The two bearings together (≈47 W) release three to four times less heat than the jaws: at $q = 1000$ W/m^2 and a heated chamber-wall area of about 0.15–0.18 m^2 (estimated from the chamber dimensions), the jaw contribution is 150–180 W. The exact distribution of the bearing heat therefore has little effect on T_{max}. The results are interpreted with the solution for a plane wall heated by the flux q on one side and cooled by convection on the other [41]:

$$T(x) = T_\infty + \frac{q}{h} + \frac{q\,x}{\lambda}, \qquad \Delta T_{wall} = \frac{q\,\delta}{\lambda} \tag{9}$$

where x is measured from the outer surface. The term $q/h = 83.3$ °C is the overheating of the outer surface above ambient; in the one-dimensional setting, it is the same for all materials and exceeds the through-wall difference for GCI and PC. Because heat conduction with a convective boundary is a linear problem (radiation was neglected), the overheating $T_{max} - T_\infty$ is proportional to the heat load. The uncertain point temperature can therefore be replaced by the critical heat flux at which the temperature limit is reached, assuming that all heat inputs scale in proportion:

$$q_{cr} = q_{ref}\,\frac{T_{lim} - T_\infty}{T_{max,FEA} - T_\infty} \tag{10}$$

2.8. Load Spectrum and Forced Vibration

In each shaft revolution, the swing jaw performs a working stroke and an idle stroke. The crushing force was approximated by a half-sine pulse, whose Fourier series is

$$F(t) = F_{max}\left[\frac{1}{\pi} + \frac{1}{2}\sin\omega t - \frac{2}{\pi}\sum_{k=1}^{\infty}\frac{\cos 2k\omega t}{4k^2 - 1}\right] \tag{11}$$

with $\omega = 2\pi n/60 = 31.42$ rad/s. Equation (11) implies a pulsating cycle ($R = \sigma_{min}/\sigma_{max} = 0$, $\sigma_a = \sigma_m = \sigma_{max}/2$) and even harmonics with amplitudes $F_{2k}/F_{max} = 2/[\pi(4k^2 - 1)]$; a fast

Fourier transform of the sampled pulse reproduced these coefficients to within 3.1×10^{-5} (relative) for $k \leq 100$. The frame was represented by an equivalent single-degree-of-freedom (SDOF) system tuned to the first mode, with the dynamic amplification factor (DAF)

$$\mathrm{DAF}(r) = \frac{1}{\sqrt{(1-r^2)^2 + (2\zeta r)^2}}, \qquad r = \frac{f}{f_1} \tag{12}$$

and the dynamic increment of the load estimated from the harmonic of order $2k^*$ nearest to f_1:

$$\frac{\Delta F}{F_{\max}} = \frac{F_{2k^*}}{F_{\max}} \mathrm{DAF}\left(\frac{2k^* f_{\mathrm{op}}}{f_1}\right) \tag{13}$$

The damping ratios were taken as $\zeta = 0.005$ (GCI), 0.035 (PC) and 0.02 (ABS). These values are assumptions consistent with the qualitative ranking of damping capacity [12,15], not measurements. Because the frequency-domain estimate (13) ignores the phases of the harmonics and the free vibration excited at the start and end of each pulse, the steady-state response was also computed in the time domain:

$$\ddot{x} + 2\zeta\omega_1\dot{x} + \omega_1^2 x = \omega_1^2 x_{\mathrm{st,max}}\, u(t), \qquad u(t) = \frac{F(t)}{F_{\max}} \tag{14}$$

Equation (14) was integrated exactly for piecewise-linear input (first-order hold) with a time step of $T_1/200$, where $T_1 = 1/f_1$, over 14 load cycles. The last cycle, by which time the start-up transient had decayed, was compared with the quasi-static response $x_{\mathrm{qs}} = x_{\mathrm{st,max}} u(t)$. Because stresses are practically independent of the material, the static deflection is inversely proportional to the modulus: $\delta_m/\delta_{\mathrm{GCI}} = E_{\mathrm{GCI}}/E_m$.

2.9. High-Cycle Fatigue

At 300 rpm, the frame accumulates 18,000 cycles per hour and reaches the base of $N_{\mathrm{D}} = 10^7$ cycles in 556 h, i.e., in about 70 eight-hour shifts. The limiting maximum stress of the pulsating cycle, $\sigma_{0\mathrm{D}}$, was obtained from mean-stress diagrams [14] with the endurance limit $\sigma_{-1\mathrm{D}} = \sigma_{-1}/K_{\mathrm{D}}$. For GCI, a brittle material, the first-quadrant Smith–Dolan locus recommended for grey cast iron [14] was used:

$$\frac{\sigma_{\mathrm{a}}}{\sigma_{-1\mathrm{D}}} = \frac{1 - \sigma_{\mathrm{m}}/\sigma_{\mathrm{u}}}{1 + \sigma_{\mathrm{m}}/\sigma_{\mathrm{u}}} \;\Rightarrow\; \sigma_{0\mathrm{D}} = \sqrt{(\sigma_{\mathrm{u}} + \sigma_{-1\mathrm{D}})^2 + 4\sigma_{\mathrm{u}}\sigma_{-1\mathrm{D}}} - (\sigma_{\mathrm{u}} + \sigma_{-1\mathrm{D}}) \tag{15}$$

where the second expression follows from the pulsating load line $\sigma_{\mathrm{a}} = \sigma_{\mathrm{m}} = \sigma_{0\mathrm{D}}/2$. For ABS, the Goodman line was used:

$$\frac{\sigma_{\mathrm{a}}}{\sigma_{-1\mathrm{D}}} + \frac{\sigma_{\mathrm{m}}}{\sigma_{\mathrm{u}}} = 1 \;\Rightarrow\; \sigma_{0\mathrm{D}} = \frac{2\sigma_{-1\mathrm{D}}\,\sigma_{\mathrm{u}}}{\sigma_{\mathrm{u}} + \sigma_{-1\mathrm{D}}} \tag{16}$$

For GCI, $\sigma_{-1} \approx 0.4\sigma_{\mathrm{u}} = 80$ MPa and $K_{\mathrm{D}} = 1.6$ (as-cast surface and size effect; the geometric stress concentration is already captured by the FEA) were assumed, which gives $\sigma_{-1\mathrm{D}} = 50$ MPa and $\sigma_{0\mathrm{D}} = 70.2$ MPa. This $\sigma_{-1\mathrm{D}}$ equals the tension–compression fatigue strength of EN-GJL-200 given in EN 1561 [33]. The Goodman line would give 80.0 MPa and is used only as a non-conservative bound. For FDM-ABS, the fatigue strength at 10^7 cycles was taken as $0.25\sigma_{\mathrm{u}} = 13.75$ MPa with $K_{\mathrm{D}} = 1$ (experimental fatigue data for FDM-ABS [25–27,35] are compared with this assumption in Section 4.3), which gives $\sigma_{0\mathrm{D}} = 22$ MPa. In the finite-life region, the Basquin relation with the reference point $\sigma_0(10^3) = 0.9\sigma_{\mathrm{u}}$ [14] was used:

$$\sigma_0(N) = \sigma_0\,(10^3)\left(\frac{N}{10^3}\right)^b, \qquad b = \frac{1}{4}\lg\frac{\sigma_{0\mathrm{D}}}{\sigma_0\,(10^3)} \tag{17}$$

which gives $b = -0.102$ for GCI and -0.088 for ABS. For PC, which has no physical endurance limit, a relation of the Aas-Jakobsen type developed for plain concrete [42] was used:

$$\frac{\sigma_{\max}}{f} = 1 - \beta(1-R)\lg N, \qquad N = 10^{(1-\sigma_{\max}/f)/\beta} \quad (R = 0) \tag{18}$$

with $\beta = 0.0685$ after Tepfers and Kutti [43]. For compression zones, the reference strength is $f = f_c = 80$ MPa (the design strength of Table 1). Tepfers [44] showed that the same relation describes the tensile fatigue of concrete, so $f = \sigma_t = 10$ MPa was used for tension zones. Applying relations calibrated on cement concrete to an epoxy-bound material is an assumption; it is checked against flexural fatigue data for an epoxy polymer concrete [45] in Section 4.3 and Appendix B (Table A4). The fatigue safety factor is $n_f = \sigma_0(N_D)/\sigma_{\max}$, and the required value is $n_{f,req} = 1.5$. For GCI and the tension zones of PC, $\sigma_{\max}$ is the largest principal-stress σ_1 at the critical point, as assumed in Section 2.5; for ABS and the compression zones of PC, it is σ_{VM}.

2.10. Admissible Crushing Force and Required Wall Thickening

Provided that $\sigma_{\max} \propto F_{cr}$ (verified in Section 3.1), the two load cases translate into an admissible crushing force for each criterion:

$$F_{adm}^{(s)} = F_{ref}\frac{\sigma_{lim}}{n_{s,req}\,\sigma_{ref}}, \qquad F_{adm}^{(f)} = F_{ref}\frac{\sigma_{0D}}{n_{f,req}\,\sigma_{ref}}, \qquad F_{ref} = 150\ \text{kN} \tag{19}$$

where σ_{ref} is the peak stress at F_{ref}. The admissible force does not depend on the contact area assumed in (1) and allows the criteria to be compared directly. When it falls short of the required force, the necessary wall thickening is estimated from plate bending theory [46]: at a constant bending moment, the stress is inversely proportional to the square of the thickness, so

$$\frac{t_{req}}{t} = \sqrt{\frac{\sigma_{ref}\,n_{s,req}}{\sigma_{lim}}}, \qquad \frac{m_{req}}{m_{GCI}} = \frac{t_{req}}{t}\,\frac{\rho_m}{\rho_{GCI}} \tag{20}$$

Uniform thickening of all walls scales the bending stiffness of all members equally, so in a bending-dominated, statically indeterminate frame the distribution of internal forces, and hence the bending moment at the peak, is preserved. The second relation in (20) is an upper estimate of mass, since local reinforcement of the peak zones requires less material. Equation (20) assumes bending-dominated peaks; if membrane stresses ($\sigma \propto 1/t$) prevailed, the required thickening would be larger. When the walls are thickened inwards to keep the outer dimensions, the change must be reconciled with the crushing chamber and the bearing seats. For a thickened PC frame, the hot-spot temperature was estimated by applying the three-dimensional-to-one-dimensional overheating ratio of the original PC frame (Section 3.3) to the solution (9) with the new wall thickness.

2.11. Modelling of Transient Heating and Thermal Stress

Heating from the cold state was described by one-dimensional conduction across a wall of thickness $\delta = 25$ mm [41]:

$$\begin{aligned} \rho c\,\frac{\partial T}{\partial t} &= \lambda\,\frac{\partial^2 T}{\partial x^2}, & T(x,0) &= T_\infty, \\ -\lambda\frac{\partial T}{\partial x}\Big|_{x=0} &= q, & -\lambda\frac{\partial T}{\partial x}\Big|_{x=\delta} &= h(T - T_\infty) \end{aligned} \tag{21}$$

where $x = 0$ is the heated inner surface. The problem was solved with an implicit finite-difference scheme (51 nodes, $\Delta t = 5$ s); a refined run (101 nodes, $\Delta t = 1$ s) changed the characteristic times by less than 0.1%, and the long-time solution reproduced the analytical steady state (9). The normalised response of the heated surface, $\Theta(t) = [T(0,t) - T_\infty]/[T(0,\infty) - T_\infty]$, was scaled to the steady-state maximum of the three-dimensional

FEA: $T_{\mathrm{hot}}(t) = T_\infty + (T_{\mathrm{max,FEA}} - T_\infty)\Theta(t)$. This assumes that the hot spot of the frame has the same time constant as the plane wall, a simplification discussed in Section 4.5. The heat-transfer regime is characterised by the Biot number $\mathrm{Bi} = h\delta/\lambda$ and the lumped time constant $\tau = \rho c\delta/h$. Thermal stresses were estimated from the solution for a plate with a linear temperature profile and restrained bending [46]:

$$\sigma_{\mathrm{th}} = \frac{E\,\alpha\,\Delta T}{2(1-\nu)} \tag{22}$$

Two estimates of ΔT were considered. The upper bound is the full temperature range over the frame from the FEA, which includes differences between distant zones. The lower bound is the through-wall difference from (9), capped at the FEA value. Both enter the combined indicator $n_{\mathrm{tm}} = \sigma_{\mathrm{lim}}/(\sigma_{\mathrm{VM,max}} + \sigma_{\mathrm{th}})$, which adds stresses of different origin and is therefore an indicator rather than a strength check.

2.12. Multi-Criteria Decision-Making Methodology

The decision matrix $X = [x_{ij}]$ contains five criteria: C1, the governing static safety factor at 150 kN (benefit); C2, the governing fatigue safety factor at 50 kN (benefit); C3, f_1 (benefit); C4, the hot-spot overheating $T_{\mathrm{max}} - T_\infty$ (cost); and C5, the frame mass (cost). Overheating rather than T_{max} was used because it scales linearly with the heat flux, so the vector-normalised criterion does not depend on the assumed q. Classical TOPSIS with vector normalisation [29] was applied:

$$\begin{aligned} r_{ij} &= \frac{x_{ij}}{\sqrt{\sum_i x_{ij}^2}}, \qquad v_{ij} = w_j\, r_{ij}, \\ S_i^{\pm} &= \sqrt{\sum_j \left(v_{ij} - v_j^{\pm}\right)^2}, \qquad C_i^* = \frac{S_i^-}{S_i^+ + S_i^-} \end{aligned} \tag{23}$$

where v^+ and v^- are the ideal and anti-ideal solutions. Two decision matrices were compared. Matrix A uses von Mises-based safety factors for all materials, as is common in FE-based material comparisons: $n_{\mathrm{s,VM}}$ at 150 kN in C1 and the compression-zone fatigue factor of PC in C2. Matrix B uses the governing criteria identified in this study: Coulomb–Mohr for GCI, the principal tensile stress for PC ($n_{\mathrm{s,t}}$ and the tensile fatigue factor) and von Mises for ABS (for GCI and PC, estimates for the assumed stress state $\sigma_1 = \sigma_{\mathrm{VM}}$, Section 2.5). Both matrices use the frequencies consistent with Table 1, i.e., the FE result for GCI and the analytical predictions by (6) for PC and ABS (Section 3.2). The base weights $w = (0.30, 0.25, 0.10, 0.15, 0.20)$ reflect the priorities of an industrial crusher and were assigned by expert judgement, i.e., they are subjective. Three checks were therefore performed: (i) one-parameter sensitivity to the mass weight w_5 over 0–0.7, with the other weights rescaled in proportion to their base values; (ii) Monte Carlo sampling of 2×10^5 weight vectors uniformly distributed on the simplex (Dirichlet distribution with unit parameters, fixed seed), in the spirit of stochastic multi-criteria acceptability analysis [32]; and (iii) variants with the frequencies of the original PC and ABS FE runs and with absolute rather than relative temperatures. A feasibility filter was applied before ranking: governing $n_{\mathrm{s}} \geq 3.0$, $n_{\mathrm{f}} \geq 1.5$ and $T_{\mathrm{max}} < T_{\mathrm{lim}}$.

2.13. Uncertainty Treatment and Reproducibility

The computed quantities carry three sources of uncertainty: discretisation ($\leq$3.5% in stress), material properties and the parameters of the analytical models. Because statistical distributions of the properties are unknown for these specific materials, a deterministic interval analysis was used instead of a probabilistic one. The key parameters were varied as follows: $K_{\mathrm{D}} = 1.4$–1.8 and the Smith–Dolan versus Goodman criterion for GCI; $\sigma_{-1}/\sigma_{\mathrm{u}} = 0.20$–$0.30$ for ABS; $f_{\mathrm{c}} = 80$–100 MPa, $\sigma_{\mathrm{t}} = 10$–20 MPa and $\beta = 0.0685 \pm 10\%$ for

PC. The ranges were chosen to test the robustness of the qualitative conclusions rather than to construct confidence intervals; a conclusion is considered robust if a criterion is met, or violated, over the whole range. Monte Carlo probabilities are reported with 95% binomial confidence intervals (half-width ≤ 0.002 for 2×10^5 samples), and a second random seed reproduced them within this interval. The analytical calculations (Equations (8)–(23)) were implemented in Python 3.12 (Python Software Foundation, Wilmington, DE, USA) (NumPy, SciPy); all numbers in Section 3 can be reproduced from Table 1 and the finite-element results in Tables 2–4.

Table 3. Natural frequencies of the frame: FE results for GCI and for the original PC and ABS runs, with frequency ratios f_i/f_1, and analytical predictions by (6) and (7). The original PC and ABS runs are superseded; the frequencies consistent with Table 1 are analytical predictions from the GCI FE solution, not FE results.

Mode	GCI, FEA, Hz (f_i/f_1)	PC, Original FE Run, Hz (f_i/f_1)	ABS, Original FE Run, Hz (f_i/f_1)
1	957.96 (1.000)	1143.5 (1.000)	443.27 (1.000)
2	1045.7 (1.092)	1240.8 (1.085)	491.99 (1.110)
3	1134.0 (1.184)	1348.6 (1.179)	530.43 (1.197)
4	1398.1 (1.459)	1667.6 (1.458)	647.58 (1.461)
5	1511.1 (1.577)	1798.7 (1.573)	702.91 (1.586)
E_{eff} by (7) at the specified ρ, GPa	110	50.1 (Table 1: 30)	3.43 (Table 1: 2.3)
f_1 consistent with Table 1, analytical prediction by (6), Hz	957.96	885.1	362.7
f_2–f_5, analytical prediction by (6), Hz	—	966/1048/1292/1396	396/429/529/572
f_1 corrected for Poisson's ratio, simplified bending/shear estimate (Section 2.6), Hz	—	876.2/899.5	375.4/349.1
Resonance margin $k_r = f_1/f_{\text{op}}$ (adopted: FEA for GCI, prediction by (6) for PC and ABS)	192	177	73

Table 4. Steady-state thermal results (FEA), one-dimensional estimate (9) and critical heat flux (10).

Quantity	GCI	PC	FDM-ABS
$T_{\max}$ (FEA), °C	55.75	89.19	111.8
$T_{\min}$ (FEA), °C	42.41	25.64	24.88
$\Delta T = T_{\max} - T_{\min}$, °C	13.34	63.55	86.92
Biot number Bi $= h\delta/\lambda$	0.006	0.30	1.76
Through-wall difference $q\delta/\lambda$ (9), °C	0.5	25.0	147.1
Heated-face temperature by (9), °C	108.8	133.3	255.4
$(T_{\max,\text{FEA}} - T_\infty)/(T_{1\text{D}} - T_\infty)$	0.37	0.59	0.38
q_{cr} for $T_{\text{lim}} = 80$ °C, W/m^2	1789	857	634
q_{cr} for $T_{\text{lim}} = 100$ °C, W/m^2	2439	1168	864

3. Results

This section reports the computed results and their immediate consequences; interpretation and comparison with the literature follow in Section 4.

3.1. Static Stress State

Peak stresses differ by no more than 18% among the three materials (18.07–21.31 MPa at 50 kN), whereas the elastic moduli differ by a factor of 48 (Table 2, Figure 2). For PC and ABS the stresses grow strictly linearly with load (ratios of 3.00 and 2.99). For GCI the ratio of 3.10 is 3% above the ideal value. A ratio above three implies a negative intercept of the $\sigma(F)$ relation (-1.0 MPa), whereas self-weight and the constant bearing load would produce a positive one, so the deviation is attributed to discretisation error ($\leq$3.5%). Self-weight amounts to at most 1.1% of the smaller crushing force and cannot explain the scatter between materials, which instead correlates with Poisson's ratio: the lowest peak stress was obtained for ABS ($\nu = 0.36$).

The peak zones—the fillets and gussets of the mounting feet and the junction between the bearing support and the side wall—coincide for all materials (Figure 2). Most of the wall volume is stressed below 4 MPa at 50 kN, so the structure uses its load-bearing capacity unevenly.

The brittle-material safety factors are estimates for the assumed stress states of Section 2.5, and within its bounds they change as follows (Table A5). For GCI, $n_{s,MC}$ falls from 9.71/3.13 at 50/150 kN to 8.41/2.71 and the fatigue factor from 3.41/1.10 to 2.95/0.95; for PC, the tensile safety factor falls from 0.47/0.16 to 0.41/0.14. The conclusions at 50 kN are unaffected: GCI keeps $n_{s,MC} \geq 8.4$ and $n_f \geq 2.9$, and PC misses the tensile requirement by a factor of 6.4–7.4. At 150 kN, GCI misses the fatigue requirement in both cases. Whether it also misses the static one ($n_{s,MC} = 3.13$ or 2.71 against 3.0) depends on the actual principal stresses and cannot be decided from these estimates, so its inadmissibility at 150 kN rests on the fatigue check alone.

All values of this section refer to the simplified load introduction of Section 2.3. A load introduction through the fixed-jaw, bearing and toggle seats would change the stress distribution, and possibly the critical locations and the principal-stress ratios at them, so the admissible forces presented in Section 3.6 cannot be transferred to it by a common scale factor; they were not recomputed for it. What does not depend on the stress field are the conditions under which each mechanism governs. For ABS, the static and the fatigue checks both use σ_{VM}, so the fatigue-governed admissible force is $2\sigma_{0D}/\sigma_{lim} = 0.80$ of the static one under any load introduction. For GCI, the same ratio is 0.70 at a critical point with $\sigma_3 \approx 0$ and grows with a compressive σ_3, reaching one only for $|\sigma_3| \approx 1.5\sigma_1$; fatigue therefore governs wherever the critical point is tension-dominated. For PC, the tensile check (4) is decisive wherever σ_1 exceeds $\sigma_t/\sigma_{lim} = 1/8$ of σ_{VM}, which holds on the tensile side of any zone in bending. Whether these conditions are met at the critical points of the real load introduction, and which admissible forces result, can only be established by an analysis with that load introduction. For orientation only: the GCI frame would meet the fatigue requirement at 150 kN if its governing peak stress were at least 27% lower than in the adopted scheme ($\kappa \leq 0.73$), or 37% lower ($\kappa \leq 0.63$) at the upper bound of σ_1.

By criterion (2), only GCI satisfies $n_{s,req} = 3$ at both loads, and the Coulomb–Mohr criterion gives the same values for $\sigma_1 \approx \sigma_{VM}$; at the upper bound $\sigma_1 = 1.155\sigma_{VM}$ it gives 8.41 and 2.71, so that GCI would then also miss the static requirement at 150 kN (Table 2). At 150 kN, ABS is at its limit state even with the optimistic strength of Table 1 ($n_{s,VM} = 1.02$, an upper bound): the peak stress of 54.1 MPa is only 2% below the tensile strength, which leaves no margin for impact loads or weak interlayer bonding. For PC, criterion (2) gives 3.75 and 1.25, but the tensile check (4) is decisive. With $\sigma_1 \approx \sigma_{VM}$, the tensile safety factor is

0.47 at 50 kN and 0.16 at 150 kN (0.41 and 0.14 at the upper bound of σ_1). A PC frame with a geometry designed for cast iron therefore fails the tensile check even in light duty. This conclusion does not hinge on the accuracy of the assumption: reaching $n_{s,t} = 1$ would require $\sigma_1 \leq 0.47\sigma_{VM}$, which is possible only for a predominantly compressive stress state, whereas a gusset in bending always has a tensile side. Nor does it hinge on the tensile strength: doubling it to 20 MPa gives $n_{s,t} = 0.94$ at 50 kN, and $n_{s,t} = 3$ would require $\sigma_t \approx 64$ MPa.

3.2. Natural Frequencies and Similarity-Law Check

The first mode of all three frames is bending of the ribbed front wall between the side walls, with the largest amplitude on the lower ribs (Figure 3). The ratios f_i/f_1 (Table 3) coincide for the three materials to within 1.7% (0.6% for PC), and the residual scatter is consistent with the different Poisson's ratios. The second consequence of (6) therefore holds: geometry, mesh and fixtures are identical in the three analyses.

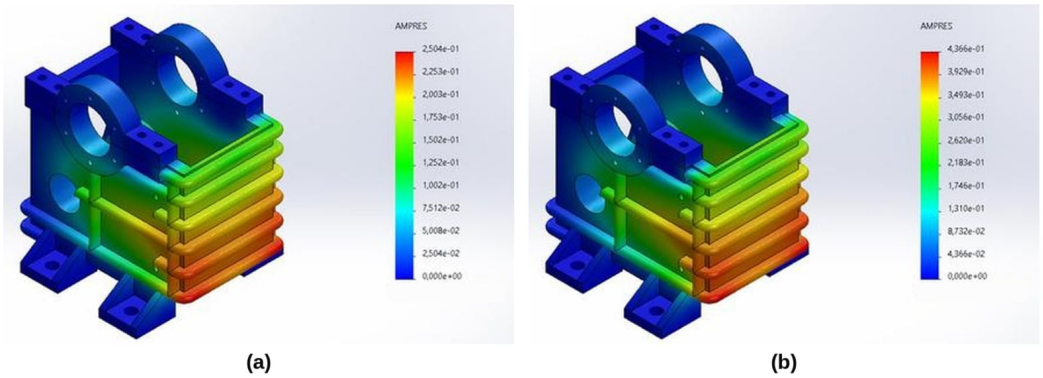


Figure 3. First mode shape (mass-normalised resultant amplitude, AMPRES): (**a**) GCI frame, 957.96 Hz; (**b**) original modal run labelled PC, 1143.5 Hz, superseded by the analytically predicted frequencies of Table 3 and shown because its amplitude was used for the density check in Section 3.2.

The first consequence holds only partly for PC and ABS. With the properties of Table 1, their frequencies should be 0.924 and 0.379 of those of GCI, whereas the modal analyses gave 1.194 and 0.463. The maximum amplitudes of the mass-normalised mode shapes (0.2504 for GCI and 0.4366 for the PC run) have a ratio of 1.744, which differs from $\sqrt{(\rho_{GCI}/\rho_{PC})} = 1.769$ by 1.5%. The density in the modal analysis therefore matched Table 1, and the discrepancy lies in the stiffness input: back-calculation by (7) gives $E_{eff} \approx 50$ GPa for PC and 3.4 GPa for ABS. In other words, the original modal runs for PC and ABS used stiffer variants of these materials than those specified in Table 1.

Since the mode shapes and frequency ratios of the three materials coincide, the frequencies consistent with Table 1 can be predicted analytically from the GCI solution via (6): $f_1 = 885.1$ Hz for PC and 362.7 Hz for ABS, i.e., $k_r = 177$ and 73. These are analytical predictions, not FE results: the modal analyses of PC and ABS were not repeated with the properties of Table 1. Relation (6) is exact for equal Poisson's ratios (Section 2.6); for the actual ones, simplified plate estimates shift the bending-dominated first mode to 876 Hz for PC and 375 Hz for ABS and a shear-dominated one to 900 and 349 Hz, i.e., into the ranges 876–900 Hz and 349–375 Hz ($k_r = 175.2$–179.9 and 69.8–75.1). These estimates do not capture the full three-dimensional behaviour of the frame. The predicted values 885.1 and 362.7 Hz were used in all subsequent calculations, so that statics, dynamics and heating share a single property set. The conclusions drawn from them do not hinge on their exact values: the resonance margin is large with either the predicted or the original frequencies, replacing one by the other changes the TOPSIS closeness coefficients by at most 0.003 (Section 3.9),

and the quasi-static formulation would remain valid down to 151 Hz for PC and 200 Hz for ABS (Section 4.2).

3.3. Steady-State Temperature Field

The GCI frame is practically isothermal: the whole frame lies within 42.4–55.8 °C, and the coolest regions are the mounting feet (Figure 4a). In the ABS frame, almost the entire outer surface stays close to ambient temperature, while heat is trapped in the heated inner walls and around the bearing seats (Figure 4c). PC is intermediate (Figure 4b). The one-dimensional model (9) overestimates the hot-spot overheating by a factor of 1.7–2.7 (Table 4) because it assumes equal heated and cooled areas. For the isothermal GCI frame, the balance $qA_{\text{in}} = hA_{\text{out}}(T - T_{\infty})$ at T = 42.4–55.8 °C gives a cooled-to-heated area ratio $A_{\text{out}}/A_{\text{in}} \approx$ 2.7–4.8, and ≈3.5 at the mean frame temperature of 49.1 °C (bearing heat neglected). This agrees in order of magnitude with the geometry: the total wall surface, estimated as $2V/\delta \approx 0.62$ m^2, is about four times the heated chamber area of 0.15–0.18 m^2.

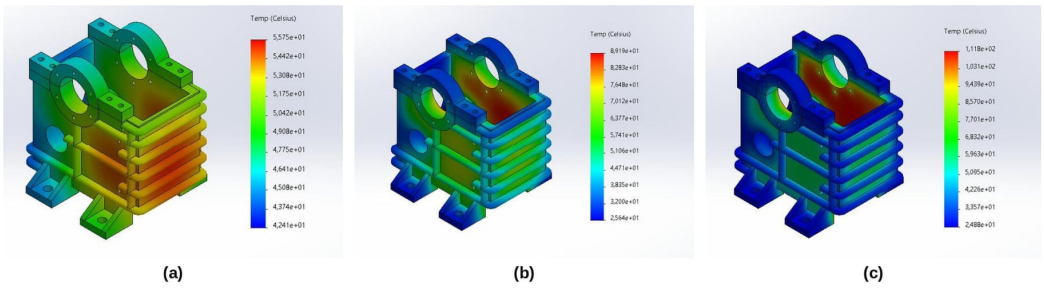


Figure 4. Steady-state temperature fields (°C) at q = 1000 W/m^2 on the chamber walls and $q_{\text{b}} \approx$ 500 W/m^2 on the bearing units (decimal comma in the software output): (**a**) GCI, 42.4–55.8 °C; (**b**) PC, 25.6–89.2 °C; (**c**) FDM-ABS, 24.9–111.8 °C.

Expressed through the critical heat flux (10), ABS exceeds an 80 °C limit already at 63% of the assumed flux (q_{cr} = 634 W/m^2) and PC at 86% (857 W/m^2), whereas GCI tolerates 1.8 times the assumed flux (1789 W/m^2). For T_{lim} = 100 °C, the critical fluxes are 864, 1168 and 2439 W/m^2, respectively. Because the thermal problem is linear, the ranking of the materials by the thermal criterion does not depend on the actual heat load: the critical fluxes stand in the ratio 1:1.35:2.82 (ABS:PC:GCI) whatever q is. Over the decade q = 300–3000 W/m^2 (Table A3), all three frames stay below 80 °C at the lower end, whereas at the upper end even GCI exceeds 100 °C. The thermal criterion thus excludes ABS above 634–864 W/m^2 and PC above 857–1168 W/m^2 (80/100 °C limits) and does not discriminate between the materials below 634 W/m^2.

3.4. Load Spectrum and Dynamic Response

Figure 5 shows the half-sine load model and its line spectrum: besides the mean value and the fundamental, only even harmonics are present, and their amplitudes fall off as $1/k^2$. At the operating frequency, the dynamic amplification is negligible (DAF $- 1 \leq 1.9 \times 10^{-4}$; Table 5, Figure 6a). The even harmonic nearest to resonance is strongly amplified, but its amplitude is only 10^{-5}–10^{-4} of F_{max} (Figure 5b). For GCI, the value DAF = 91.8 is very sensitive to f_1, because the 960 Hz harmonic lies only 0.2% from it; the product $Q{\cdot}F_{2k^*}$, which does not depend on the exact position of the harmonic, is a more robust measure and remains below 0.31% of F_{max} for all materials and both estimates of f_1.

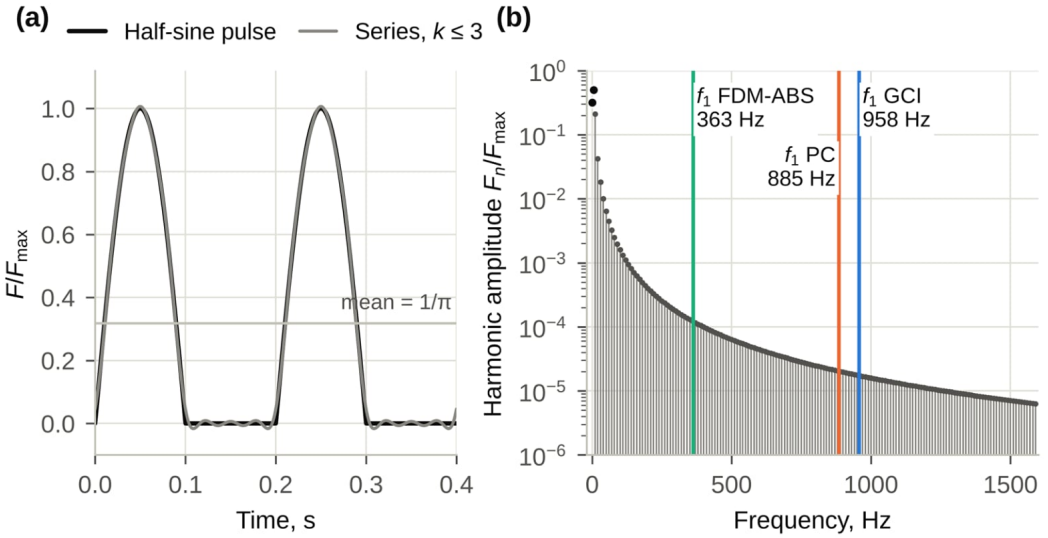


Figure 5. Crushing load model: (**a**) half-sine pulse over two shaft revolutions and its Fourier series (11) truncated after the third even harmonic; (**b**) harmonic amplitudes F_n/F_{max} with the first natural frequencies of the three frames (FEA for GCI; analytical predictions by (6) for PC and ABS).

Table 5. Dynamic response of the equivalent SDOF system (12)–(14). For PC and ABS, values are given for f_1 of the superseded original FE runs/predicted analytically by (6) for the properties of Table 1.

Quantity	GCI	PC	FDM-ABS
ζ (assumed)	0.005	0.035	0.020
$r = f_{op}/f_1$	5.22×10^{-3}	$4.37 \times 10^{-3}/5.65 \times 10^{-3}$	$1.13 \times 10^{-2}/1.38 \times 10^{-2}$
DAF at 5 Hz	1.000027	1.000019/1.000032	1.00013/1.00019
$Q = 1/(2\zeta)$	100	14.3	25
Harmonic nearest to f_1, Hz	960	1140/890	440/360
F_{2k^*}/F_{max}	1.73×10^{-5}	$1.22 \times 10^{-5}/2.01 \times 10^{-5}$	$8.22 \times 10^{-5}/1.23 \times 10^{-4}$
DAF at that harmonic	91.8	14.3/14.0	23.6/23.6
$\Delta F/F_{max}$ by (13)	1.59×10^{-3}	$1.75 \times 10^{-4}/2.82 \times 10^{-4}$	$1.94 \times 10^{-3}/2.89 \times 10^{-3}$
$Q \cdot F_{2k^*}/F_{max}$	1.73×10^{-3}	$1.75 \times 10^{-4}/2.87 \times 10^{-4}$	$2.06 \times 10^{-3}/3.07 \times 10^{-3}$
Peak-response increment, time domain (14), %	0.12	0.002/0.003	0.05/0.12
Largest deviation from the quasi-static response, %	0.53	0.44/0.57	1.14/1.39
Relative static deflection δ/δ_{GCI}	1.0	3.67	47.8

The time-domain solution of (14) confirms and refines these frequency-domain estimates (Figure 6b). The steady-state peak response exceeds the quasi-static peak by at most 0.12% (GCI and ABS) and by 0.003% for the well-damped PC. The largest instantaneous deviation from the quasi-static response, 0.5–1.4% of the static peak, comes from free vibrations excited by the slope discontinuities of the half-sine pulse at its start and end, i.e., where the load is close to zero, and it decays before the load peak. The quasi-static formulation of Section 3.1 is therefore justified for the smooth load model (11). The static deflection of the ABS frame is 47.8 times that of the GCI frame; at the same force, the contribution of

the frame to the opening of the discharge gap under load grows by the same factor, which would widen the product size distribution.

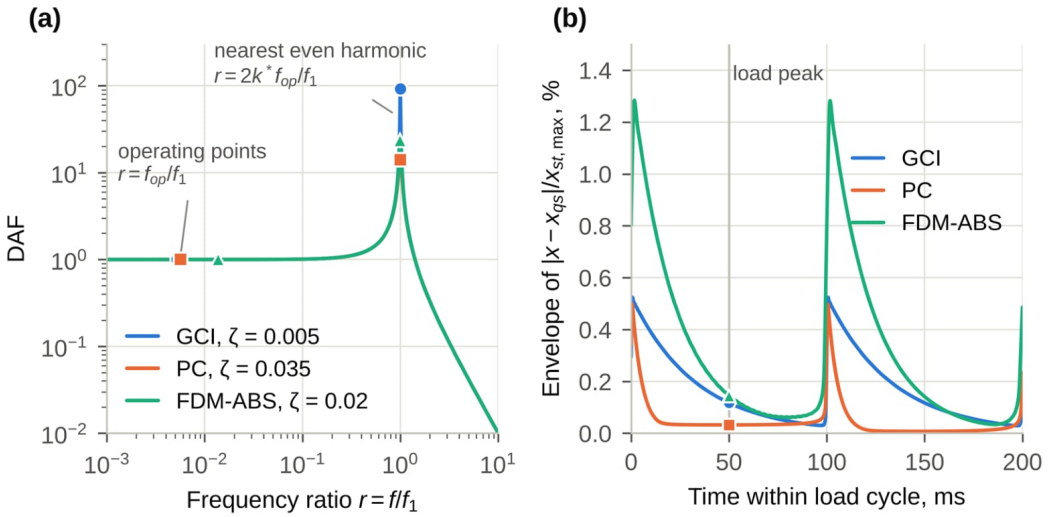


Figure 6. Dynamic response of the equivalent SDOF system: (**a**) DAF curves for the assumed damping ratios with the operating points ($r = f_{op}/f_1$) and the even harmonics nearest to resonance; (**b**) envelope of the deviation of the steady-state response from the quasi-static response over one load cycle.

3.5. Fatigue

The qualitative fatigue conclusions (Tables 6 and 7, Figure 7) hold over the entire parameter range, whereas the quantitative life of PC in compression at 150 kN is uncertain by three orders of magnitude. Table 6 therefore reports only this range; the robust result is that the life is 15–22,000 times shorter than the 10^7-cycle base. In tension zones, PC fails the fatigue requirement even at 50 kN (n_f = 0.22–0.53), consistent with its static tensile deficit. For GCI at 150 kN, the peak stress lies below the fatigue limit, so the predicted life is unlimited, but the safety factor of 1.01–1.21 falls short of the required 1.5; even the non-conservative Goodman line gives at most 1.39.

Table 6. High-cycle fatigue assessment ($R = 0$, $N_D = 10^7$, $n_{f,req} = 1.5$) with the base parameters; $\sigma_{max} = \sigma_1$ for GCI and the tension zones of PC (estimate for the assumed stress state $\sigma_1 = \sigma_{VM}$; upper bound in Table A5), σ_{VM} otherwise.

Quantity	GCI	PC	FDM-ABS
Mean-stress criterion	Smith–Dolan (15)	Relation (18)	Goodman (16)
Limiting stress $\sigma_0(10^7)$, MPa	70.2	41.6 (compression)/5.2 (tension)	22.0 [a]
n_f at 50 kN	3.41	1.95 (compression)/0.24 (tension)	1.22 [a]
n_f at 150 kN	1.10	0.65 (compression)	0.41 [a]
Predicted life at 150 kN	>10^7 cycles ($\sigma_{max} < \sigma_{0D}$)	4.5×10^2–6.9×10^5 cycles (0.025–38 h, parameter ranges of Table 7), compression zones	<10^3 cycles ($\sigma_{max} > 0.9\sigma_u$)
$n_f \geq 1.5$ at 50/150 kN	met/not met	not met (tension)	not met/not met

[a] Upper bound (on-axis properties, Section 2.2); with the measured strengths of printed ABS, n_f at 50 kN is 0.19–0.68 (Table A2).

Table 7. Sensitivity of the fatigue conclusions to uncertain parameters.

Material	Varied Parameter	Range of Result	Conclusion Robust?
GCI	K_D = 1.4–1.8, Smith–Dolan	n_f(150 kN) = 1.01–1.21; n_f(50 kN) = 3.12–3.75	Yes: always < 1.5 at 150 kN and >1.5 at 50 kN
GCI	K_D = 1.4–1.8, Goodman (non-conservative)	n_f(150 kN) = 1.14–1.39	Yes: still < 1.5
ABS	σ_{-1}/σ_u = 0.20–0.30	n_f(50 kN) = 1.01–1.40	Yes: always < 1.5
ABS	σ_u = 8.4–30.8 MPa (printed, Table A2)	n_f(50 kN) = 0.19–0.68	Yes: always < 1.5
PC, compression zones	f_c = 80–100 MPa, β = 0.0617–0.0754	N(150 kN) = 4.5 × 10^2–6.9 × 10^5 cycles (0.025–38 h)	Yes: always ≪ 10^7
PC, compression zones	Same	$\sigma_0(10^7)$ = 37.8–56.8 MPa; n_f(50 kN) = 1.77–2.67	Yes: always > 1.5
PC, tension zones	σ_t = 10–20 MPa, β = 0.0617–0.0754	n_f(50 kN) = 0.22–0.53	Yes: always < 1.5
PC, thickened frame (preliminary estimate, Section 3.7)	β = 0.0617–0.0769 (incl. epoxy PC data, Table A4)	n_f(50 kN) = 1.39–1.71	No: <1.5 for β > 0.0714

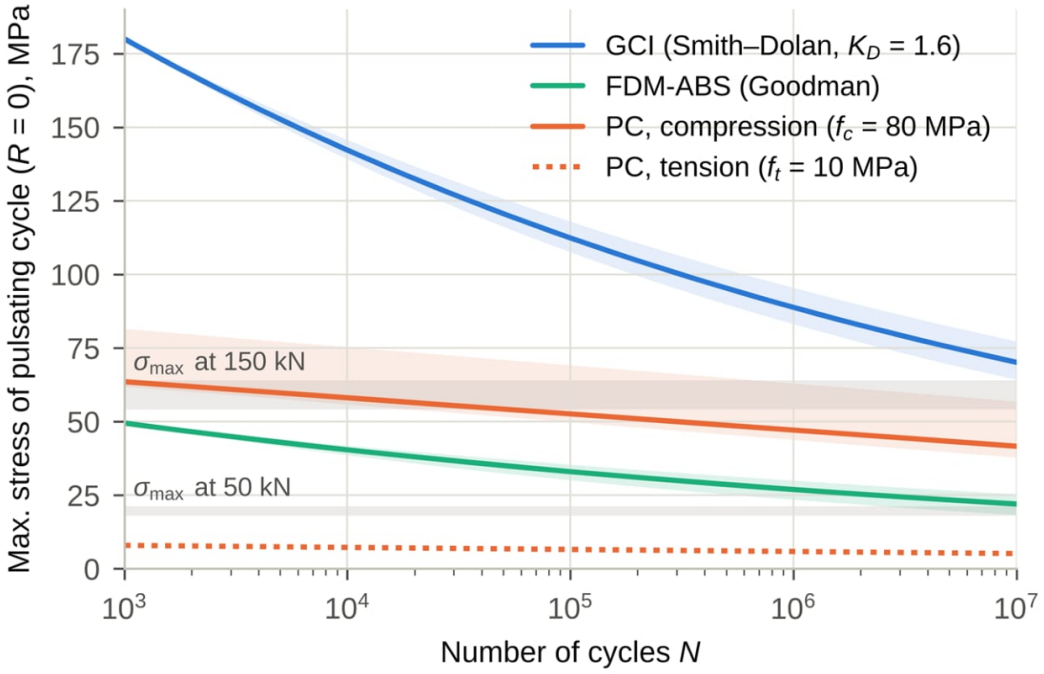


Figure 7. Fatigue-strength curves for the pulsating cycle (R = 0): GCI (Smith–Dolan with Basquin extension; band for K_D = 1.4–1.8), FDM-ABS (Goodman; band for σ_{-1}/σ_u = 0.20–0.30) and PC (relation (18) in compression with a band for f_c = 80–100 MPa and β ± 10%, and in tension). Grey bands show the peak stresses of the three frames at 50 and 150 kN.

3.6. Admissible Crushing Force and Governing Mechanism

For GCI, the fatigue limit on the crushing force is 30% below the static one, and for ABS, it is 20% below (Table 8, Figure 8). For PC in the original geometry, the tensile strength governs: the admissible force of 7.8 kN, and 8.1 kN by tensile fatigue, is an order of magnitude below the values for compression (62.5 kN) and compression fatigue (65 kN).

The wall thickening required by (20), a preliminary plate-theory estimate, is 2.53 for 50 kN and 4.38 for 150 kN (Section 3.7). With the measured strengths of printed ABS, its governing admissible force falls to 6–23 kN (Table A2).

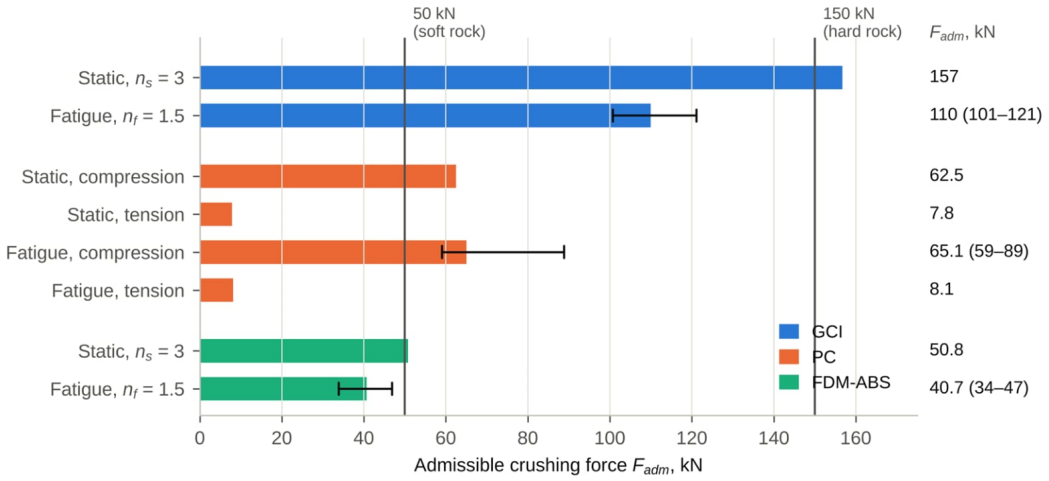


Figure 8. Admissible crushing force by static and fatigue criteria (Equation (19)); whiskers and values in parentheses show the ranges of Table 7. Vertical lines mark the crushing forces for soft (50 kN) and hard (150 kN) rock.

Table 8. Admissible crushing force by Equation (19), kN (see also Figure 8).

Criterion	GCI	PC	FDM-ABS
Static, von Mises (PC: compression zones), $n_s = 3$	157	62.5	50.8 [a]
Static, Coulomb–Mohr (GCI)/principal tension (PC), $n_s = 3$, estimated for $\sigma_1 \approx \sigma_{VM}$ (in brackets: $\sigma_1 = 1.155\sigma_{VM}$)	157 (136)	7.8 (6.8)	—
Limit state, $n_s = 1$	470	23.4 (tension)	152 [a]
Fatigue, $n_f = 1.5$, base parameters	110 (95)	65.1 (compression)/8.1 (7.0) (tension)	40.7 [a]
Fatigue, $n_f = 1.5$, ranges of Table 7	101–121 (Goodman: 114–139)	59–89 (compression)	34–47 [a]
Fatigue, $n_f = 1.5$, measured strengths of printed ABS (Table A2)	—	—	6.2–22.8
Thermal criterion at $q = 1000$ W/m^2	met	met for $T_{lim} = 100$ °C, not met for 80 °C	not met [1]
Governing value	110 (95) (fatigue)	7.8 (6.8) (tension, original geometry)	40.7 (fatigue) [a] and thermal failure

[1] At the assumed heat flux, which in the model does not depend on the crushing force. [a] Upper bound for ABS (Section 2.2; Table A2). Values for GCI and for the tension zones of PC are estimates for the assumed stress state $\sigma_1 \approx \sigma_{VM}$; values in brackets: upper bound $\sigma_1 = 1.155\sigma_{VM}$ (Section 2.5); further values in Table A5. All values refer to the simplified load introduction of Section 2.3 (see Section 3.1).

Of the three materials, GCI comes closest to 150 kN. Its force deficit of 27% can be removed by lowering the peak stress in the fillets from 63.8 to 46.8 MPa, which, by (20), corresponds to a local section thickening of about 17%. Alternatively, a stronger iron grade

can be used: with the same endurance ratio and K_D, EN-GJL-300 (σ_u = 300 MPa) gives n_f = 1.65 at 150 kN without geometric changes, whereas EN-GJL-250 gives 1.37. At the upper bound, $\sigma_1 = 1.155\sigma_{VM}$ (Section 2.5), the deficit grows to 37%; the peak stress has to fall from 73.7 to 46.8 MPa, which requires about 26% local thickening, and EN-GJL-300 gives n_f = 1.43, below the requirement (Table A5).

3.7. Material-Adapted Polymer Concrete Frame: Preliminary Analytical Estimate

The estimates in this section rest on plate scaling (20) and have not been verified by an FE analysis of the modified geometry; they indicate trends, not verified performance. By (20), uniform thickening of the PC walls by a factor of 2.53 to about 63 mm would lower the bending stress at the peak 6.4-fold and restore $n_{s,t}$ = 3 at 50 kN (Table 9, Figure 9a). The estimated tensile fatigue factor, 1.56, exceeds the requirement by only 4%, a margin smaller than the uncertainty of relation (18) for an epoxy-bound material: $n_f \geq 1.5$ requires $\beta \leq 0.0714$, whereas the slope that matches flexural fatigue data of an epoxy polymer concrete at the lowest tested stress level is 0.072–0.077 (Section 4.3, Table A4), for which n_f = 1.39–1.48. The fatigue adequacy of the thickened frame is therefore not established. Its mass would rise to at most 45.4 kg, 19% below that of the GCI frame (68% below in the original geometry); the mass advantage disappears at about 77 kN (Figure 9b), and at 150 kN the thickened frame (× 4.38) would be 40% heavier than the cast-iron one. At the upper bound $\sigma_1 = 1.155\sigma_{VM}$ (Section 2.5), the required thickening grows to × 2.72 (68 mm), the mass to 48.8 kg (13% below that of the GCI frame) and the mass advantage disappears at about 66 kN, whereas the fatigue factor stays at 1.56, because the thickening is sized to the same peak stress (Table A5). Thickening would also stiffen the walls: for a uniformly thickened plate, the bending frequencies grow approximately in proportion to the thickness, so the resonance margin can only increase, whereas the effect on the temperature field is adverse, as shown next.

Table 9. GCI frame versus PC frames of the original geometry and with walls thickened by Equation (20) for a crushing force of 50 kN; the σ_1-based safety factors are estimates for $\sigma_1 \approx \sigma_{VM}$ (upper bound $\sigma_1 = 1.155\sigma_{VM}$: Table A5), and all values for the thickened frame are preliminary analytical estimates, not verified by FE analysis.

Quantity	GCI (Original)	PC (Original)	PC (Thickened × 2.53)
Wall thickness, mm	25	25	63
Frame mass, kg	56.2	17.9	≤45.4 [1]
Governing static safety factor at 50 kN	9.71 (Coulomb–Mohr)	0.47 (tension)	3.00 (tension)
Governing fatigue safety factor at 50 kN	3.41	0.24 (tension)	1.56 (tension) [3]
T_{max} at q = 1000 W/m², °C	55.8 (FEA)	89.2 (FEA)	≈112 [2]
q_{cr} for T_{lim} = 100 °C, W/m²	2439	1168	≈864 [2]
Quality factor Q	100	14.3	14.3

[1] Upper estimate for uniform thickening. [2] Estimate obtained by applying the three-dimensional-to-one-dimensional overheating ratio of the original PC frame (Table 4) to Equation (9) with δ = 63 mm. [3] 1.39–1.71 for β = 0.0617–0.0769 (Tables 7 and A4); $n_f \geq 1.5$ requires $\beta \leq 0.0714$.

Thickening, however, has a thermal cost. The conduction drop across a 63 mm wall with λ = 1 W/(m·K) is 63 °C instead of 25 °C, and the estimated hot-spot temperature rises from 89 to about 112 °C at q = 1000 W/m² (Figure 9c). The thickened frame thus exceeds even the 100 °C limit of a hot-cured binder. It remains admissible only if the actual heat flux is below about 860 W/m², or if heat paths such as steel inserts are provided at the bearing

seats. Along the design curve of Figure 9c, the 100 °C limit is reached already at about 23 kN. These temperatures are estimates: they rely on the overheating ratio of the original frame and require confirmation by a thermal FEA of the thickened geometry.

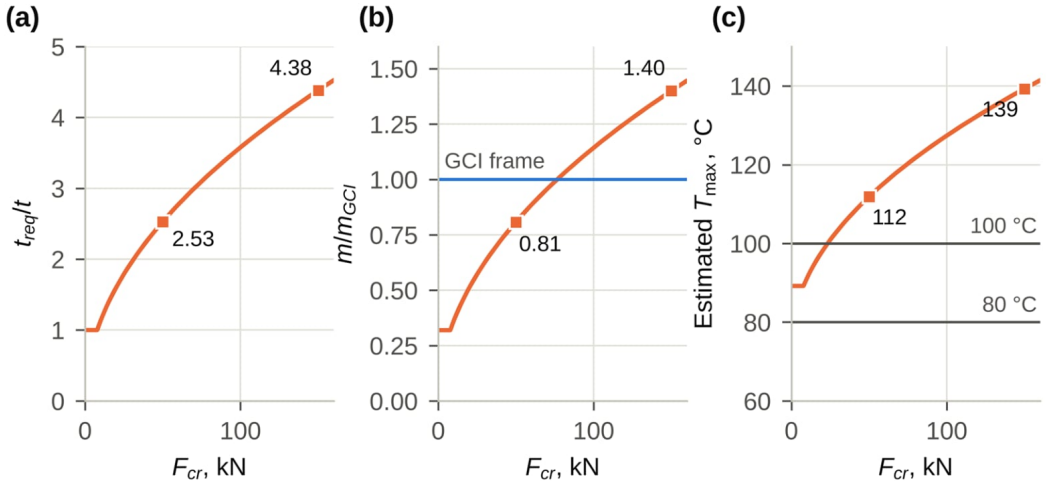


Figure 9. Material-adapted PC frame as a function of the crushing force (preliminary analytical estimate by Equation (20), not verified by FE analysis; tensile criterion $n_{s,t} = 3$): (**a**) required wall-thickness ratio; (**b**) frame mass relative to the GCI frame; (**c**) estimated hot-spot temperature at $q = 1000$ W/m^2 with the limits of cold- and hot-cured binders.

3.8. Transient Heating and Thermal Stress

The time constants of the finite-difference model (Table 10, Figure 10) agree with the lumped estimate for GCI and PC (115 and 80–81 min), as expected for Bi ≤ 0.3. For ABS (Bi = 1.76), the heated surface warms faster than the mean wall temperature: it reaches 63% of the steady state in 68 min, 80 °C in 69 min and 100 °C in 2.5 h, i.e., within the first shift. PC reaches 80 °C after 2.7 h and settles near 89 °C. For PC, the outcome of the thermal-stress check depends on the choice of ΔT: the upper bound $\sigma_{th} = 14.7$ MPa exceeds the tensile strength by 47%, whereas the lower bound, 5.8 MPa, is 58% of it. For GCI, the upper bound overestimates the thermal stress by an order of magnitude: the 13 °C range is spread over the whole frame, whereas the through-wall difference is only 0.5 °C.

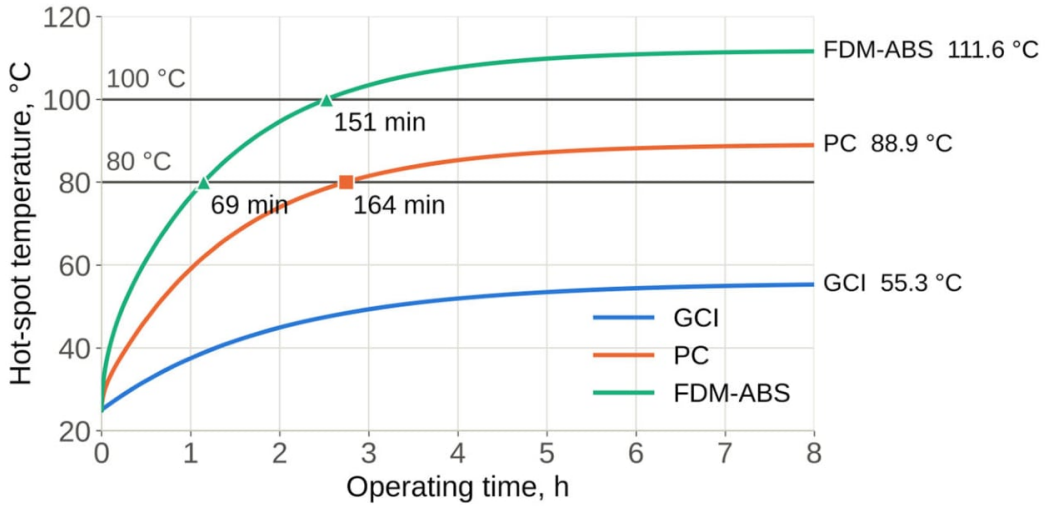


Figure 10. Transient heating of the hot spot from the cold state (one-dimensional model (21) scaled to the FEA steady state) with the 80 °C and 100 °C limits.

Table 10. Transient heating of the hot spot (21) and thermal stresses (22).

Quantity	GCI	PC	FDM-ABS
$\tau = \rho c\delta/h$, min	115	80	51
Time to 63%/95% of the steady state, min	115/345	81/257	68/235
Time to 80 °C, min	not reached	164	69
Time to 100 °C, min	not reached	not reached	151
Hot-spot temperature after 8 h, °C	55.3	88.9	111.6
σ_{th}, lower bound (through-wall ΔT), MPa	0.39	5.77	14.06
σ_{th}, upper bound (FEA ΔT), MPa	10.41	14.67	14.06
σ_{th}/σ_t (upper bound)	0.05	1.47	0.26
n_{tm} at 50 kN (lower–upper σ_{th})	9.53–6.45	2.95–2.22	1.71
n_{tm} at 150 kN (lower–upper σ_{th})	3.12–2.70	1.15–1.02	0.81

3.9. Multi-Criteria Ranking

At the base weights, both matrices rank GCI first (Table 11, Figure 11). The choice of strength measure, however, changes the runner-up. With von Mises-based safety factors (matrix A), PC is second ($C^* = 0.433$) and takes the lead when w_5 exceeds 0.267. With the governing criteria (matrix B), PC drops to last place ($C^* = 0.281$), and ABS takes the lead when $w_5 > 0.315$. Under random weights, GCI ranks first for 66% (A) and 75% (B) of the weight sets. Changing the PC and ABS frequencies by +29% and +22% (the size of the original modal error) changes C^* by at most 0.003, and using absolute temperatures instead of overheating changes it by at most 0.005. With the upper bound $\sigma_1 = 1.155\sigma_{VM}$ in matrix B, the closeness coefficients become 0.686, 0.284 and 0.458, GCI ranks first for 74% of the weight sets, and ABS takes the lead when $w_5 > 0.301$ (base case: 0.690, 0.281, 0.424, 75% and 0.315); the ranking does not change. In both matrices, an alternative that fails the feasibility constraints ranks first for 25–34% of the random weight vectors.

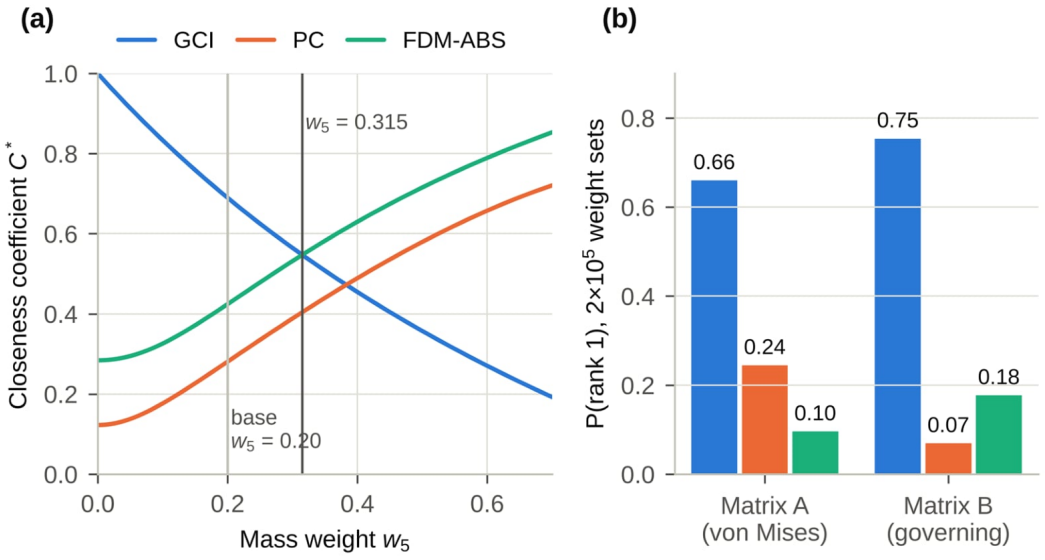


Figure 11. TOPSIS ranking without the feasibility filter: (**a**) closeness coefficients versus the mass weight w_5 for decision matrix B (governing criteria); (**b**) probability of ranking first over 2×10^5 random weight vectors for matrices A and B (half-widths of the 95% confidence intervals ≤ 0.002).

The feasibility filter changes the interpretation of the TOPSIS results substantially. At 50 kN, the original GCI configuration satisfies the adopted static and fatigue requirements and is not limited by the assumed thermal conditions. The original PC configuration fails the tensile-strength criterion, whereas FDM-ABS fails the fatigue requirement and exceeds the assumed thermal service-temperature limit. Accordingly, GCI is the only feasible alternative

among the three original configurations at 50 kN. At 150 kN, however, the original GCI frame also fails the required fatigue safety factor, with nf = 1.10 < 1.50. Therefore, none of the three original material–geometry combinations can be classified as fully admissible at 150 kN under the adopted criteria.

Table 11. Robustness of the TOPSIS ranking to the decision matrix and the weights (without the feasibility filter).

Decision Matrix	C^* GCI/PC/ABS (Base Weights)	P(Rank 1) GCI/PC/ABS, 2×10^5 Weight Sets	w_5 at Which GCI Loses First Place (New Leader)
A: von Mises-based	0.599/0.433/0.401	0.660/0.244/0.096	0.267 (PC)
B: governing criteria	0.690/0.281/0.424	0.754/0.069/0.177	0.315 (ABS)

Criteria values. A: $n_{s,VM}$(150 kN) = 3.13/1.25/1.02; n_f(50 kN) = 3.41/1.95/1.22. B: n_s(150 kN) = 3.13/0.16/1.02; n_f(50 kN) = 3.41/0.24/1.22 (GCI and PC: estimates for $\sigma_1 = \sigma_{VM}$). Both: f_1 = 957.96/885.1/362.7 Hz (GCI: FEA; PC and ABS: predicted by (6)); $T_{max} - T_\infty$ = 30.8/64.2/86.8 °C; m = 56.2/17.9/8.2 kg. Half-widths of the 95% confidence intervals of $P \leq 0.002$. ABS values of n_s and n_f are upper bounds (Section 2.2).

The analytically adapted PC frame provides a potential alternative for the 50 kN case, but its predicted mechanical and thermal performance remains conditional on the wall-thickening assumptions, its fatigue margin lies within the uncertainty of relation (18) (Section 4.3), and it requires independent numerical verification. A two-alternative TOPSIS comparison of the original GCI frame with the adapted PC frame (base weights; criteria of matrix B, with $n_{s,t}$ = 1.00 at 150 kN, n_f = 1.56, $T_{max} - T_\infty$ = 86.9 °C and m = 45.4 kg for the adapted frame, whose f_1 was conservatively kept at 885 Hz) gives C* = 0.89 for GCI and 0.11 for the adapted frame. It should therefore be interpreted as a provisional ranking of an FE-analysed reference configuration against an analytically projected design. Similarly, the preference transition at a mass weight above about 0.67 is conditional on the assumed properties of the adapted PC frame. The feasibility filter must be reapplied using updated results once the modified geometries and their loading conditions have been validated.

4. Discussion

4.1. Stress Invariance and Its Consequences for Material Selection

A scatter of peak stresses of at most 18% despite a 48-fold difference in modulus is an expected consequence of linear elasticity [39], not a peculiarity of this design. It nevertheless has a practical corollary. For a fixed geometry and load introduction, the whole strength comparison reduces to the ratios of the limiting properties of the materials, and the FEA is needed only once to obtain the geometric influence coefficients. This is what allowed the two load cases to be converted into admissible forces for every criterion (Table 8).

The reverse side of the same fact is a systematic handicap for the lightweight materials. With identical geometry, PC and ABS do not exploit their only advantage, low density, which allows thicker sections. For a plate in bending, stiffness scales with Et^3 and the bending stress with $1/t^2$ [46]. At equal stiffness the frame mass is therefore inversely proportional to the index $E^{1/3}/\rho$, and at an equal safety factor to $\sigma^{1/2}/\rho$ [47]. The stiffness index is 0.67 for GCI, 1.35 for PC and 1.26 for ABS ($GPa^{1/3}\cdot m^3/t$). An equally stiff PC wall must be 1.54 times thicker than the cast-iron one and is then half as heavy (mass ratio 0.49). PC also outperforms GCI on the fatigue-strength index ${\sigma_{0D}}^{1/2}/\rho$ (2.81 versus 1.16), but not on the tensile-strength index ${\sigma_t}^{1/2}/\rho$ (1.37 versus 1.96), which is the one that governs. A PC frame designed for the material—thicker walls, compression instead of tension in the critical zones, steel inserts at the bearing units—could thus compete with cast iron in light duty, although this has so far been estimated only preliminarily by plate theory (Section 3.7). This agrees with machine-tool practice, where polymer concrete beds are designed massive and

with embedded steel elements rather than copying cast geometry [12,19]. The preliminary estimate of Section 3.7 indicates the price of this approach in a crusher: the low conductivity that keeps machine-tool beds thermally stable [12] traps the heat of the bearings and the crushing zone, as observed for steel-reinforced epoxy granite beds [20], and the thicker the wall, the hotter the bearing seats. For ABS the same scaling gives a wall 3.6 times thicker (about 90 mm), which would aggravate the heat trapping further.

4.2. Similarity-Law Verification as a Quality-Control Tool

Comparative studies of materials on a single geometry have a valuable property: their results are linked by relations (6) and (7), exact for equal Poisson's ratios, which can be checked without experiments or additional analyses. The linearity of stresses in load and the invariance of the mode-frequency ratios held to within 3% and 1.7%, respectively, and the 18% scatter of peak stresses among the materials is consistent with their different Poisson's ratios. The absolute PC and ABS frequencies of the original modal runs deviated from (6) by +29% and +22%. Without the check, one could conclude that a PC frame has a higher natural frequency than a cast-iron frame of the same geometry, which is impossible for the property values of Table 1, since $\sqrt{(E/\rho)}$ of PC is lower than that of GCI.

The pattern of the deviations points to their cause. A stiffness error with the correct density is supported by the amplitude ratio, whereas a partial reassignment of the assembly would have required the same fraction of unchanged stiffness for PC and ABS (≈25% and ≈1% were found), and a change of contact conditions is excluded by the coinciding frequency ratios. The frequencies consistent with Table 1 can therefore be predicted from the GCI solution. Relation (6) is exact for the discretised eigenproblem with identical geometry, mesh, fixtures and Poisson's ratio (Section 2.6). For the actual Poisson's ratios, simplified plate relations put the deviation of a repeated analysis at −1.0% to +1.6% for PC and −3.7% to +3.5% for ABS; only a repeated FE analysis could confirm this, and the predicted frequencies are therefore not presented as FE results. The methodological lesson extends beyond this problem: when the material is varied parametrically, checking (6) and (7) should be a mandatory acceptance step, because the error caught here would otherwise have reversed the frequency ranking of PC and GCI.

The rigid fixture at the bolt holes idealises the foundation and therefore overestimates the frequencies. Instead of assuming a particular mounting stiffness, the tolerable frequency shift can be bounded from the load spectrum. The resonant increment cannot exceed $Q{\cdot}F_{2k}/F_{max}$, and with $F_{2k}/F_{max} = 2/[\pi(4k^2 - 1)]$ this bound stays below 1% as long as $f_1 \geq 2k_{min}{\cdot}f_{op}$, where $k_{min} = ½[1 + 2Q/(0.01\pi)]^{1/2}$. This gives $f_1 \geq 399$ Hz for GCI ($Q = 100$), 151 Hz for PC ($Q = 14.3$) and 200 Hz for ABS ($Q = 25$), so the first frequencies of the frames could fall by about 58%, 83% and 45%, respectively, before the quasi-static formulation of Section 3.1 would be affected by more than 1%. The rigid-body modes of the whole machine on its mounts are a different matter. They are governed by the mounting stiffness and the mass of the complete crusher rather than by the frame material, and they are excited by unbalanced inertia forces, whereas the crushing force is self-equilibrated within the frame (Section 2.3). They must be checked for the actual installation, as the supporting-structure failures reported by Rusiński et al. [10] illustrate.

4.3. Why Fatigue, Not Static Strength, Limits the Frame

The frame accumulates the 10^7-cycle base in 556 h of operation, i.e., within the first months of service. For the pulsating cycle, the limiting stress is only $0.35\sigma_u$ for GCI (Smith–Dolan) and $0.40\sigma_u$ for ABS (Goodman). With the adopted safety factors ($n_{s,req} = 3$, $n_{f,req} = 1.5$), the fatigue constraint is therefore 30% (GCI) and 20% (ABS) more restrictive than the static one. This ratio follows directly from the assumed ratios σ_{0D}/σ_u and the

required safety factors, not from the FEA. It shows that checking a frame by the static safety factor alone, as is common in engineering FEA of crusher parts [9], systematically overestimates the admissible load; the supporting-structure damage reported by Rusiński et al. [10] was fatigue cracking.

Each fatigue model rests on different evidence and has its own direction of bias. For GCI, multiaxial fatigue tests showed that failure is governed by tension and that the Smith–Watson–Topper criterion gives the best predictions [13]; the fatigue check therefore uses the largest principal-stress σ_1 at the critical point rather than σ_{VM}; σ_1 is assumed and bounded as in Section 2.5. The adopted component endurance limit, $\sigma_{-1D} = 50$ MPa, equals the tension–compression fatigue strength of EN-GJL-200 and lies well below its bending fatigue strength of 90 MPa [33]; an additional as-cast surface factor would lower it and strengthen the conclusion that fatigue governs. The Smith–Dolan locus adds a further 12% of conservatism relative to the Goodman line.

For ABS, the available evidence points the same way. Tension–tension tests on printed ABS at $R = 0.1$ gave lives of 1.1×10^4–1.8×10^4 cycles at 45–50% of the ultimate strength for 0°, 45° and 90° rasters [35], whereas the Basquin line adopted here predicts 0.8×10^6–2.6×10^6 cycles at these stress levels. The printed strength itself is 1.8–6.6 times lower than the 55 MPa used (Table A2), and heating from 50 to 70 °C sharply reduces the fatigue life of FDM-ABS [28], while the computed hot zone of the frame reaches 111.8 °C. Every ABS fatigue value in Tables 6–8 is therefore an upper bound; with the measured printed strengths, n_f at 50 kN falls to 0.19–0.68.

For PC, relation (18) was calibrated on cement concrete in compression [42,43] and extended to tension by Tepfers [44], and its transfer to an epoxy-bound material is the weakest assumption of the fatigue analysis. Fatigue data for epoxy polymer concretes come from bending tests: on paving mixes at stress levels of 0.2–0.5 of the static strength [23] and on an epoxy polymer concrete composite in three-point bending at $R = 0.1$ [45]. Table A4 compares the latter with (18). At $S = 0.75$–0.80, the reported design lives for 10–25% failure probability exceed the predictions of (18), but at the lowest level tested, $S = 0.65$, they are two to four times shorter, and the slope that would match them, $\beta = 0.072$–0.077, lies at or beyond the upper end of the range in Table 7. Relation (18) is thus not demonstrably conservative for epoxy-bound mixes in the high-cycle range. This does not affect the conclusions on the original PC frame, which misses the tensile criteria by a factor of three to six, but it leaves the fatigue adequacy of the thickened frame open (Section 3.7). In all three cases, a refined model can only strengthen the conclusion that fatigue limits the admissible force.

For the GCI frame at 150 kN, the deficit is about 27% in force. Removing it requires the peak stress in the fillets of the mounting feet to be lowered from 63.8 to 46.8 MPa. This is achievable with larger fillet radii or thicker gussets (about 17% local thickening by (20)) or with a stronger iron grade such as EN-GJL-300 (Section 3.6). If the stress state at the critical point is biaxial, the required thickening rises to about 26% and EN-GJL-300 alone no longer suffices (Section 3.6, Table A5).

4.4. Thermal Behaviour: Critical Heat Flux Instead of a Point Temperature

The weakest input of the thermal analysis is the heat flux $q = 1000$ W/m^2, which is not supported by measurements. Formulating the result through the critical heat flux (10) moves the uncertainty from the result to an input that can be measured on a real crusher (Section 4.6). ABS exceeds its temperature limit already at 63% of the assumed flux, whereas cast iron withstands almost twice the assumed flux even with a nominal 80 °C limit (Table 4). The parameter study of Table A3 shows the same ordering over the whole decade of plausible fluxes.

For PC, thermal and mechanical factors interact. The low conductivity that benefits a machine-tool bed [12] creates gradients and tensile thermal stresses in a crusher with local heat sources, and these stresses act on a material that is weak in tension. The range σ_{th} = 5.8–14.7 MPa brackets the tensile strength of 10 MPa, so thermal cracking cannot be ruled out without a coupled thermo-mechanical analysis. Heating also changes the fracture behaviour of epoxy PC [22]. The suitability of a given mix at 89 °C can be judged only from the glass transition temperature of its binder, which for cold-cured resins may lie below this value. Two design limits were therefore considered: 80 °C for a cold-cured and 100 °C for a hot-cured binder. With the latter, the computed T_{max} = 89.2 °C leaves a margin of about 11 °C in the original geometry, and, according to the preliminary estimate of Section 3.7, this margin is consumed by the thickening needed for strength.

4.5. Limitations

The results were obtained in a comparative setting. Their limits of applicability, and the way each limit was handled, are as follows:

- Comparative nature. All materials were analysed with identical geometry, loads and fixtures, so the ratios between them are more reliable than the absolute values. The results were converted into admissible forces (19), which do not depend on the assumed contact area.
- Idealised load path and fixtures. The idealisation is the same for all materials, but it is not neutral: the real load introduction (through the fixed-jaw, bearing and toggle seats, Section 2.3) would change the stress distribution and possibly the critical locations and principal-stress ratios. The absolute admissible forces are therefore valid only for the adopted scheme, and the governing mechanisms were identified for it; Section 3.1 gives the conditions under which they would persist. Owing to stress invariance, one analysis with the real load introduction would serve all three materials, but such an analysis belongs to the design verification of a specific crusher and was not part of this comparative study. The rigid-foundation assumption overestimates the natural frequencies, but the quasi-static formulation remains valid as long as f_1 stays above 399, 151 and 200 Hz for GCI, PC and ABS (Section 4.2); resonance of the supporting structure is a known concern for jaw crushers [10] and must be checked for the actual installation.
- Linear isotropic elasticity. The anisotropy of FDM-ABS [24,25] and the loss of polymer properties on heating [28] would tighten the conclusions. ABS is excluded even with the most favourable isotropic properties, so accounting for these effects does not change the outcome. The sensitivity analysis with measured strengths of printed ABS (Table A2) quantifies this: n_s at 50 kN does not exceed 1.70 for any printed orientation.
- Smooth load model. Broadband impact components from fracturing lumps and uncrushable objects are not part of (11). For such inputs the quality factor bounds the resonant amplification, and here, the high damping of PC (Q = 14.3 versus 100 for GCI) is an advantage. Quantifying this requires a transient dynamic analysis with a measured force spectrum.
- Analytically derived quantities. Two inputs were not computed by the FE analysis. The principal stresses at the critical point were not extracted from the FE solution but assumed ($\sigma_1 \approx \sigma_{VM}$, $\sigma_3 \approx 0$) and bounded ($\sigma_1 \leq 1.155\sigma_{VM}$, Section 2.5); all safety factors and admissible forces of GCI and of the PC tension zones are therefore estimates for these stress states, and the static check of GCI at 150 kN cannot be decided from them (Section 3.1). The PC and ABS frequencies are analytical predictions from the GCI FE solution by (6), not FE results; the effect of the different Poisson's ratios on them was estimated only from simplified plate relations (at most 3.7%, Section 2.6), which do not represent the three-dimensional behaviour of the frame. The conclusions based on

these frequencies tolerate far larger errors: the quasi-static formulation would remain valid for first frequencies about 45% (ABS) and 83% (PC) lower (Section 4.2). The mass, temperature and fatigue factor of the adapted PC frame remain analytical estimates by plate theory and require a dedicated FE analysis (static, modal and thermal) of the modified geometry before any design use. Equation (20) assumes bending-dominated peak stresses; membrane action would increase the required thickening and thus strengthen the conclusions on mass and temperature.

- Thermal formulation. Since the actual heat flux depends on the material crushed and on the operating mode, the conclusions are stated through the critical flux (10), which applies to any measured q. The one-dimensional heating model gives the correct order of the warm-up time and agrees with the lumped estimate for Bi ≤ 0.3. Table A3 gives the hot-spot temperatures over $q = 300$–3000 W/m^2.
- TOPSIS weights. Their subjectivity was mitigated by Monte Carlo sampling and by the feasibility filter, which reduces the dependence of the outcome on weighting and normalisation noted in [30,31].

4.6. Proposed Experimental Validation

To convert the comparative conclusions into absolute design values, a minimal validation programme is proposed in which each item addresses a specific assumption:

1. Strain gauging of the mounting-foot fillets and bearing supports on an operating crusher with a cast-iron frame, to check the load path and the actual force spectrum (idealised load path; smooth load model).
2. Experimental modal analysis (impact hammer) of frames or scale models, to obtain f_1 and ζ (Section 4.2; smooth load model).
3. Thermocouples and infrared thermography of the bearing units and walls, to determine the actual heat flux and compare it with q_{cr} from (10).
4. Fatigue tests of PC specimens under pulsating tension and bending, and of FDM-ABS at 80–100 °C in the raster and build orientations of the frame, to obtain the parameters of (15)–(18) (linear isotropic elasticity; analytically derived quantities).

4.7. Assessment of the Scientific Evidence Supporting the Main Findings

Table 12 separates the main statements of this study by the type of evidence behind them.

Table 12. Evidence status of the main statements.

Statement	Status	Basis
Stresses are practically material-independent and linear in load	FE result, supported by elasticity theory	Table 2
Resonance margin $k_r \geq 69.8$; dynamic increment at the load peak $\leq 0.12\%$	Computed from the FE frequency of GCI and the analytical predictions for PC and ABS; tolerates a drop of f_1 by 45–83% (Section 4.2)	Tables 3 and 5
f_1 of PC and ABS is predicted at 876–900 and 349–375 Hz	Analytical prediction from the GCI FE solution by (6), not an FE result; exact for equal Poisson's ratios, whose effect was estimated by simplified plate relations	Equation (6), Section 2.6, Table 3
Fatigue limits the admissible force of GCI and ABS	Computed for the adopted load scheme (GCI: estimate for the assumed stress states); robust to the parameters and the mean-stress criterion; persists for another load introduction under the conditions of Section 3.1	Tables 7 and 8, Section 3.1

Table 12. *Cont.*

Statement	Status	Basis
PC in the original geometry fails the tensile check	Estimate with $\sigma_1 \approx \sigma_{VM}$; holds for $\sigma_1 > 0.47\sigma_{VM}$ and $\sigma_t < 21$ MPa	Table 2, Section 3.1
Life of PC compression zones at 150 kN is 15–22,000 times below 10^7 cycles	Robust computed result	Table 7
Thickened PC meets the static requirement at 50 kN with 13–19% less mass than GCI; its fatigue adequacy is open	Preliminary analytical estimate (plate theory), not verified by FE; fatigue margin within model uncertainty	Equation (20), Tables 9, A4 and A5
Thickened PC exceeds 100 °C at $q = 1000$ W/m^2	Estimate by scaling of the overheating ratio; requires thermal FEA	Table 9, Figure 9c
ABS overheats	Computed result for $q > 634$–864 W/m^2	Equation (10), Table 4
ABS admissible forces are upper bounds	Computed: 1.8–6.6 times lower with measured printed strengths	Table A2
Risk of thermal cracking in PC	Estimate: $\sigma_{th} = 5.8$–14.7 MPa at $\sigma_t = 10$ MPa	Table 10
The original modal discrepancy was an input error	Interpretation supported by the amplitude ratio and the coinciding frequency ratios; corrected values are analytical predictions by (6)	Sections 2.6 and 4.2, Table 3

5. Conclusions

A comparative computational framework was applied to a single-toggle jaw crusher frame of fixed geometry made of grey cast iron (GCI), epoxy polymer concrete (PC) or FDM-printed ABS. Within the adopted geometry, material data and idealised loading, the main results are as follows.

1. Governing mechanisms. Fatigue, not static strength, limits GCI and ABS, and tension limits PC. With required safety factors of 3.0 (static) and 1.5 (fatigue), the admissible crushing force is about 110 kN for GCI and at most 41 kN for ABS, an upper bound that falls to 6–23 kN with measured strengths of printed ABS; the original PC geometry is limited to about 8 kN. The GCI and PC values are estimates for an assumed stress state at the critical point ($\sigma_1 = \sigma_{VM}$, $\sigma_3 = 0$) and fall to 95 and 6.8 kN for the most unfavourable one ($\sigma_1 = 1.155\sigma_{VM}$). All values refer to the simplified load introduction; a realistic one would change the stress distribution, so they need verification for it. Fatigue would remain governing for ABS under any load introduction and for GCI wherever its critical point is tension-dominated (Section 3.1).
2. Admissibility at 50 and 150 kN. Only the original GCI frame meets all criteria at 50 kN, and none of the original frames does at 150 kN. Removing the GCI fatigue deficit at 150 kN ($n_f = 1.10$, or 0.95 for the most unfavourable stress state) would require local thickening of the mounting feet by about 17%, or 26% in that case; EN-GJL-300 suffices only if σ_1 is close to σ_{VM} ($n_f = 1.65$ versus 1.43). Both measures need FE verification.
3. Thermal limits. The thermal criterion separates the materials independently of the uncertain heat flux: the critical fluxes for an 80 °C limit are 1789, 857 and 634 W/m^2 for GCI, PC and ABS. The reference flux of 1000 W/m^2 corresponds to 1.4–3.6% of the installed power entering the frame walls.
4. Modal behaviour. The first natural frequency of the GCI frame is 958 Hz. For PC and ABS, the frequencies consistent with the specified properties were predicted analytically from it by the similarity law, which is exact for identical geometry, mesh, fixtures and Poisson's ratio: 876–900 and 349–375 Hz, where the ranges are a simplified estimate of the effect of the different Poisson's ratios; these are analytical predictions, not FE

results. The resulting resonance margins ($\geq$69.8) and a dynamic increment at the load peak below 0.12% justify the quasi-static formulation for the smooth load model. A similarity-law check, recommended as a routine acceptance test for comparative FE studies, exposed an input error in the original PC and ABS modal runs.

5. Multi-criteria ranking. Applying the feasibility constraints before TOPSIS is essential: without them, an inadmissible alternative ranks first for 25–34% of random weight vectors.

Practical implications. Plate-theory estimates suggest that a PC frame designed for the material, with walls 2.5–2.7 times thicker, could meet the static requirement at 50 kN with 13–19% less mass than GCI. Its fatigue margin, however, lies within the uncertainty of the fatigue model, and its estimated hot-spot temperature ($\approx$112–115 °C) exceeds the binder limit, so such a design would need heat paths and FE verification. Grey cast iron remains the most defensible baseline for this frame; FDM-printed ABS is suitable only for non-load-bearing prototypes and teaching models.

Author Contributions: Conceptualisation, A.K., D.B. and J.S.; methodology, A.K. and D.Y.; software, A.K. and D.B.; validation, J.S.; formal analysis, D.B. and K.Y.; investigation, D.Y.; writing—original draft preparation, A.K., J.S. and K.Y.; writing—review and editing, D.Y.; visualisation, D.Y.; supervision, D.Y. and K.Y.; project administration, D.B.; funding acquisition, K.Y. All authors have read and agreed to the published version of the manuscript.

Funding: This research received no external funding.

Institutional Review Board Statement: Not applicable.

Informed Consent Statement: Not applicable.

Data Availability Statement: The original contributions presented in this study are included in the article. Further inquiries can be directed to the corresponding authors.

Conflicts of Interest: The authors declare no conflicts of interest.

Abbreviations

The following abbreviations are used in this manuscript:

ABS	Acrylonitrile butadiene styrene
CAD	Computer-aided design
DAF	Dynamic amplification factor
DEM	Discrete element method
FDM	Fused deposition modelling
FE, FEA	Finite-element, finite-element analysis
GCI	Grey cast iron
MCDM	Multi-criteria decision-making
PC	Polymer concrete
SDOF	Single degree of freedom
TOPSIS	Technique for Order of Preference by Similarity to Ideal Solution

Appendix A

Table A1 lists the symbols used in this paper; subscripts are explained where the symbols are introduced.

Table A1. Nomenclature.

Symbol	Meaning, Unit
A_c	Projected contact area of the crushing force, m^2

Table A1. *Cont.*

Symbol	Meaning, Unit
a, L	Distances from the eccentric axis to the crushing-force resultant and to the toggle contact, m
b	Basquin exponent
c	Specific heat, J/(kg·K)
C^*	TOPSIS closeness coefficient
E, E_{eff}	Young's modulus and effective modulus by (7), GPa
f_1, f_i	First and i-th natural frequencies, Hz
f_{op}	Shaft rotation frequency, Hz
f, f_{c}	Reference strength in (18); design compressive strength of PC, MPa
F_{cr}, F_{adm}	Crushing force; admissible crushing force, kN
h	Convective heat-transfer coefficient, W/(m^2·K)
k_{r}	Resonance margin f_1/f_{op}
K_{D}	Fatigue-strength reduction factor
m	Frame mass, kg
n	Shaft speed, rpm
n_{s}, n_{f}	Static and fatigue safety factors (subscripts VM, MC, t: von Mises, Coulomb–Mohr, principal tension)
n_{tm}	Combined thermo-mechanical indicator
N, N_{D}	Number of cycles; base number of cycles (10^7)
P_{f}	Failure probability
q, q_{cr}	Heat flux; critical heat flux, W/m^2
Q	Quality factor $1/(2\zeta)$
r	Frequency ratio f/f_1
R	Stress ratio $\sigma_{\min}/\sigma_{\max}$
R_{e}, R_{t}	Reactions at the eccentric-shaft bearings and at the toggle seat, kN
S	Stress level $\sigma_{\max}/f$ in (18)
t, δ	Wall thickness, mm
T, T_{lim}, T_∞	Temperature; service-temperature limit; ambient temperature, °C
V	Frame volume, m^3
w_j	Criterion weights in TOPSIS
α	Coefficient of thermal expansion, K^{-1}
β	Slope of the fatigue relation (18)
ζ	Damping ratio
κ	Ratio of the peak stresses for the real and the simplified load introduction
λ	Thermal conductivity, W/(m·K)
ν	Poisson's ratio
ρ	Density, kg/m^3
σ_{VM}, σ_1, σ_3	Von Mises and principal stresses, MPa
σ_{t}, σ_{c}, σ_{u}, σ_{lim}	Tensile, compressive, ultimate and design strengths, MPa
σ_{-1}, $\sigma_{-1\mathrm{D}}$	Fully reversed endurance limit of the material and of the component, MPa
$\sigma_{0\mathrm{D}}$	Limiting maximum stress of the pulsating cycle at N_{D}, MPa

Table A1. *Cont.*

Symbol	Meaning, Unit
σ_{th}	Thermal stress, MPa
τ	Lumped thermal time constant, min

Appendix B

Tables A2–A4 and support Sections 2.2, 2.5, 2.7, 3.1, 3.3, 3.7 and 4.3. All quantities follow from the FE results of Tables 2 and 4 by relations (2)–(4), (10), (16), (19) and (20), or from the cited experimental data; Table A5 rests in addition on the assumed stress states of Section 2.5.

Table A2. Sensitivity of the ABS assessment to the tensile strength of printed material (peak stresses of Table 2; fatigue by (16) with $\sigma_{-1} = 0.25\sigma_u$; admissible forces by (19)).

Material and Orientation	σ_t, MPa	$n_{s,VM}$ at 50/150 kN	n_f at 50 kN	F_{adm} Static/Fatigue, kN
Adopted in Table 1 (upper bound)	55	3.04/1.02	1.22	50.8/40.7
ABS-M30, on edge (XZ), yield [36]	30.8	1.70/0.57	0.68	28.5/22.8
ABS-M30, upright (ZX), yield [36]	27.5	1.52/0.51	0.61	25.4/20.3
ABS P400, 0° raster [35]	23.08	1.28/0.43	0.51	21.3/17.1
ABS P400, +45°/−45° raster [35]	15.71	0.87/0.29	0.35	14.5/11.6
ABS P400, 45° raster [35]	10.61	0.59/0.20	0.23	9.8/7.8
ABS P400, 90° raster [35]	8.37	0.46/0.15	0.19	7.7/6.2

Required values: $n_s \geq 3$ and $n_f \geq 1.5$. The elastic properties of printed ABS depend negligibly on raster and build orientation [34], so the peak stresses of Table 2 apply to all rows.

Table A3. Hot-spot temperature T_{max} (°C) versus the chamber-wall heat flux q, scaled linearly from the FEA results of Table 4 with all heat inputs in proportion, and the corresponding share of the installed drive power.

q, W/m²	Share of 5–11 kW, %	GCI	PC	PC, Thickened × 2.53	FDM-ABS
300	0.4–1.1	34.2	44.3	51.1	51.0
500	0.7–1.8	40.4	57.1	68.4	68.4
1000	1.4–3.6	55.8	89.2	111.9	111.8
2000	2.7–7.2	86.5	153.4	198.7	198.6
3000	4.1–10.8	117.2	217.6	285.6	285.4
q_{cr} for 80/100 °C, W/m²	—	1789/2439	857/1168	633/864	634/864

Values above the service limit T_{lim} of a material are formal, because the linear scaling and the room-temperature properties no longer apply there. The thickened PC frame is the plate-theory estimate of Section 3.7. Share = qA_{in}/P for A_{in} = 0.15–0.18 m² and P = 5–11 kW.

Table A4. Flexural fatigue of an epoxy polymer concrete composite (three-point bending, $R = 0.1$ [45]) compared with relation (18). N_{10}, N_{25}: design lives for failure probabilities of 10% and 25% reported in [45]; $N_{(18)}$: prediction of (18) with $\beta = 0.0685$ and $R = 0.1$; β_{10}, β_{25}: slopes for which (18) passes through N_{10} and N_{25}.

$S = \sigma_{max}/f$	N_{10}, Cycles	N_{25}, Cycles	$N_{(18)}$, Cycles	β_{10}/β_{25}
0.80	3487	5126	1754	0.063/0.060
0.75	47,574	74,508	11,354	0.059/0.057
0.70	70,609	129,317	73,482	0.069/0.065
0.65	113,969	233,912	475,565	0.077/0.072

According to the preliminary estimate of Section 3.7, the thickened PC frame meets $n_f \geq 1.5$ only for $\beta \leq 0.0714$.

Table A5. Sensitivity of the brittle-material results to the stress state at the critical point: base case $\sigma_1 = \sigma_{VM}$ and upper bound $\sigma_1 = 1.155\sigma_{VM}$ with $\sigma_3 = 0$ (Section 2.5). All values are estimates for these assumed stress states; the principal stresses were not extracted from the FE solution.

Quantity	Base Case, $\sigma_1 = \sigma_{VM}$	Upper Bound, $\sigma_1 = 1.155\sigma_{VM}$	Used in
σ_1 at 50/150 kN, GCI; PC, MPa	20.6/63.8; 21.3/64.0	23.8/73.7; 24.6/73.9	Table 2
$n_{s,MC}$ of GCI at 50/150 kN	9.71/3.13	8.41/2.71	Table 2
$n_{s,t}$ of PC at 50/150 kN	0.47/0.16	0.41/0.14	Table 2
n_f of GCI at 50/150 kN	3.41/1.10	2.95/0.95	Table 6
n_f of GCI at 150 kN, parameter ranges of Table 7	1.01–1.21	0.87–1.05	Table 7
n_f of PC, tension zones, at 50 kN	0.24	0.21	Table 6
F_{adm} of GCI: static (3)/limit state/fatigue, kN	157/470/110	136/407/95	Table 8
F_{adm} of PC in tension: static/limit state/fatigue, kN	7.8/23.4/8.1	6.8/20.3/7.0	Table 8
Local thickening of the GCI feet for $n_f = 1.5$ at 150 kN	17%	26%	Section 3.6
n_f at 150 kN with EN-GJL-250/EN-GJL-300	1.37/1.65	1.19/1.43	Section 3.6
Thickening of the PC walls for $n_{s,t} = 3$ at 50/150 kN	×2.53/×4.38	×2.72/×4.71	Section 3.7, Table 9
Mass of the thickened PC frame at 50 kN, kg (relative to GCI)	45.4 (−19%)	48.8 (−13%)	Table 9
Force at which the PC mass advantage disappears, kN	77	66	Figure 9b
Hot-spot temperature of the thickened PC frame, °C	111.9	114.6	Table 9
TOPSIS matrix B: C* of GCI/PC/ABS	0.690/0.281/0.424	0.686/0.284/0.458	Table 11
TOPSIS matrix B: GCI first, % of weight sets; w_5 at which GCI loses first place	75; 0.315	74; 0.301	Section 3.9

The upper bound applies to GCI and to the tension zones of PC; ABS and the compression zones of PC are assessed with σ_{VM} and are not affected. The fatigue factor of the thickened PC frame (1.56) does not change because the thickening is sized to the same peak stress. Values for the thickened frame are plate-theory estimates (Section 3.7).

References

1. Wills, B.A.; Finch, J.A. *Wills' Mineral Processing Technology*, 8th ed.; Butterworth-Heinemann: Oxford, UK, 2016.
2. Johansson, M.; Bengtsson, M.; Evertsson, M.; Hultén, E. A fundamental model of an industrial-scale jaw crusher. *Miner. Eng.* **2017**, *105*, 69–78. [CrossRef]
3. Legendre, D.; Zevenhoven, R. Assessing the energy efficiency of a jaw crusher. *Energy* **2014**, *74*, 119–130. [CrossRef]
4. Abuhasel, K.A. A comparative study of regression model and the adaptive neuro-fuzzy conjecture systems for predicting energy consumption for jaw crusher. *Appl. Sci.* **2019**, *9*, 3916. [CrossRef]
5. Barrios, G.K.; Jiménez-Herrera, N.; Fuentes-Torres, S.N.; Tavares, L.M. DEM simulation of laboratory-scale jaw crushing of a gold-bearing ore using a particle replacement model. *Minerals* **2020**, *10*, 717. [CrossRef]
6. Xiong, Y.; Gan, J.; Chen, W.; Ou, T.; Zhao, G.; Wu, D. Application of multibody dynamics and bonded-particle GPU discrete element method in modelling of a gyratory crusher. *Minerals* **2024**, *14*, 774. [CrossRef]
7. Mosnegutu, E.; Barsan, N.; Chitimus, D.; Ciubotariu, V.; Bibire, L.; Mirilă, D.; Jasiński, M.; Sporea, N.; Petre, I.C. Kinematic analysis of the jaw crusher drive mechanism: A different mathematical approach. *Processes* **2025**, *13*, 2226. [CrossRef]
8. Mosnegutu, E.; Tomozei, C.; Irimia, O.; Ciubotariu, V.; Mirila, D.; Panainte-Lehadus, M.; Jasiński, M.; Sporea, N.; Petre, I.C. The influence of the geometric configuration of the drive system on the motion dynamics of jaw crushers. *Processes* **2025**, *13*, 2498. [CrossRef]

9. Murithi, M.; Keraita, J.N.; Obiko, J.O.; Mwema, F.M.; Wambua, J.M.; Jen, T.C. Optimisation of the swinging jaw design for a single toggle jaw crusher using finite element analysis. *Int. J. Interact. Des. Manuf.* **2024**, *18*, 6351–6358. [CrossRef]
10. Rusiński, E.; Moczko, P.; Pietrusiak, D.; Przybylek, G. Experimental and numerical studies of jaw crusher supporting structure fatigue failure. *Stroj. Vestn. J. Mech. Eng.* **2013**, *9*, 556–563. [CrossRef]
11. Evertsson, M.; Quist, J.; Bilock, A.; Jareteg, K. Influence of feeding condition on crusher performance and fatigue life. In Proceedings of the Comminution '23, Cape Town, South Africa, 17–20 April 2023.
12. Möhring, H.-C.; Brecher, C.; Abele, E.; Fleischer, J.; Bleicher, F. Materials in machine tool structures. *CIRP Ann.* **2015**, *64*, 725–748. [CrossRef]
13. John, E.; Boxall, J.; Collins, R.; Bowman, E.; Susmel, L. Multiaxial fatigue of water pipe grey cast iron. *Int. J. Fatigue* **2024**, *178*, 108002. [CrossRef]
14. Budynas, R.G.; Nisbett, J.K. *Shigley's Mechanical Engineering Design*, 10th ed.; McGraw-Hill Education: New York, NY, USA, 2015.
15. Orak, S. Investigation of vibration damping on polymer concrete with polyester resin. *Cem. Concr. Res.* **2000**, *30*, 171–174. [CrossRef]
16. Bruni, C.; Forcellese, A.; Gabrielli, F.; Simoncini, M. Hard turning of an alloy steel on a machine tool with a polymer concrete bed. *J. Mater. Process. Technol.* **2008**, *202*, 493–499. [CrossRef]
17. Kwon, S.; Ahn, S.; Koh, H.-I.; Park, J. Polymer concrete periodic meta-structure to enhance damping for vibration reduction. *Compos. Struct.* **2019**, *215*, 385–390. [CrossRef]
18. Cao, P.; Liang, G.; Chai, X.; Liu, Q.; Lv, M. Effects of aggregate gradation, content, and size range on the mechanical and damping properties of polymer concrete for precision machine tool beds. *Constr. Build. Mater.* **2025**, *491*, 142834. [CrossRef]
19. Venugopal, P.R.; Dhanabal, P.; Thyla, P.R.; Mohanraj, S.; Nataraj, M.; Ramu, M.; Sonawane, H. Design and analysis of epoxy granite vertical machining centre base for improved static and dynamic characteristics. *Proc. Inst. Mech. Eng. Part L J. Mater. Des. Appl.* **2020**, *234*, 481–495. [CrossRef]
20. Ramana, M.V.; Thyla, P.R.; Subramanian, E.; Chinnuraj, S. Thermal investigations on a CNC lathe fitted with a dynamically enhanced steel-reinforced epoxy granite bed. *Stroj. Vestn. J. Mech. Eng.* **2023**, *69*, 169–184. [CrossRef]
21. Li, X.; Gu, J.; Xu, Y.; Li, S.; Zhang, R. Review of component materials and diverse applications of polymer concrete. *Materials* **2025**, *18*, 2745. [CrossRef] [PubMed]
22. Elalaoui, O. Effect of short fibers on fracture properties of epoxy-based polymer concrete exposed to high temperatures. *Polymers* **2023**, *15*, 1078. [CrossRef] [PubMed]
23. Ren, S.; Hu, X. Fatigue properties and its prediction of polymer concrete for the repair of asphalt pavements. *Polymers* **2022**, *14*, 2941. [CrossRef] [PubMed]
24. Ahn, S.-H.; Montero, M.; Odell, D.; Roundy, S.; Wright, P.K. Anisotropic material properties of fused deposition modeling ABS. *Rapid Prototyp. J.* **2002**, *8*, 248–257. [CrossRef]
25. Ziemian, S.; Okwara, M.; Ziemian, C.W. Tensile and fatigue behavior of layered acrylonitrile butadiene styrene. *Rapid Prototyp. J.* **2015**, *21*, 270–278. [CrossRef]
26. Yankin, A.; Serik, G.; Danenova, S.; Alipov, Y.; Temirgali, A.; Talamona, D.; Perveen, A. Optimization of fatigue performance of FDM ABS and nylon printed parts. *Micromachines* **2023**, *14*, 304. [CrossRef] [PubMed]
27. Bakhtiari, H.; Aamir, M.; Tolouei-Rad, M. Effect of 3D printing parameters on the fatigue properties of parts manufactured by fused filament fabrication: A review. *Appl. Sci.* **2023**, *13*, 904. [CrossRef]
28. He, F.; Khan, M. Effects of printing parameters on the fatigue behaviour of 3D-printed ABS under dynamic thermo-mechanical loads. *Polymers* **2021**, *13*, 2362. [CrossRef] [PubMed]
29. Hwang, C.-L.; Yoon, K. *Multiple Attribute Decision Making: Methods and Applications*; Lecture Notes in Economics and Mathematical Systems; Springer: Berlin/Heidelberg, Germany, 1981; Volume 186. [CrossRef]
30. Jahan, A.; Edwards, K.L. A state-of-the-art survey on the influence of normalization techniques in ranking: Improving the materials selection process in engineering design. *Mater. Des.* **2015**, *65*, 335–342. [CrossRef]
31. Chakraborty, S. TOPSIS and Modified TOPSIS: A comparative analysis. *Decis. Anal. J.* **2022**, *2*, 100021. [CrossRef]
32. Lahdelma, R.; Salminen, P. SMAA-2: Stochastic multicriteria acceptability analysis for group decision making. *Oper. Res.* **2001**, *49*, 444–454. [CrossRef]
33. *EN 1561:2011*; Founding—Grey Cast Irons. CEN: Brussels, Belgium, 2011.
34. Cantrell, J.T.; Rohde, S.; Damiani, D.; Gurnani, R.; DiSandro, L.; Anton, J.; Young, A.; Jerez, A.; Steinbach, D.; Kroese, C.; et al. Experimental characterization of the mechanical properties of 3D-printed ABS and polycarbonate parts. *Rapid Prototyp. J.* **2017**, *23*, 811–824. [CrossRef]
35. Ziemian, C.W.; Cipoletti, D.E.; Ziemian, S.N.; Okwara, M.N.; Haile, K.V. Monotonic and cyclic tensile properties of ABS components fabricated by additive manufacturing. In Proceedings of the 25th Annual International Solid Freeform Fabrication Symposium, Austin, TX, USA, 4–6 August 2014; pp. 525–541.
36. Stratasys. *ABS-M30 Data Sheet (MDS_FDM_ABS-M30_A4_0920a)*; Stratasys: Eden Prairie, MN, USA, 2020.

37. Kępczak, N.; Pawłowski, W. Application of mineral casting for machine tools beds. *Mech. Mech. Eng.* **2013**, *17*, 285–289.
38. NETZSCH-Gerätebau GmbH. ABS: Acrylonitrile-Butadiene-Styrene Copolymer. Available online: https://analyzing-testing.netzsch.com/en/polymers-netzsch-com/commodity-thermoplastics/abs-acrylonitrile-butadiene-styrene-copolymer (accessed on 16 November 2026).
39. Timoshenko, S.P.; Goodier, J.N. *Theory of Elasticity*, 3rd ed.; McGraw-Hill: New York, NY, USA, 1970.
40. Numbi, B.P.; Zhang, J.; Xia, X. Optimal energy management for a jaw crushing process in deep mines. *Energy* **2014**, *68*, 337–348. [CrossRef]
41. Incropera, F.P.; DeWitt, D.P.; Bergman, T.L.; Lavine, A.S. *Fundamentals of Heat and Mass Transfer*, 7th ed.; Wiley: Hoboken, NJ, USA, 2011.
42. Hsu, T.T.C. Fatigue of plain concrete. *ACI J. Proc.* **1981**, *78*, 292–305. [CrossRef] [PubMed]
43. Tepfers, R.; Kutti, T. Fatigue strength of plain, ordinary, and lightweight concrete. *ACI J. Proc.* **1979**, *76*, 635–652. [CrossRef] [PubMed]
44. Tepfers, R. Tensile fatigue strength of plain concrete. *ACI J. Proc.* **1979**, *76*, 919–934. [CrossRef] [PubMed]
45. Bedi, R.; Singh, S.P.; Chandra, R. Design fatigue lives of polypropylene fibre reinforced polymer concrete composites. *J. Mater. Eng. Struct.* **2014**, *1*, 99–109.
46. Timoshenko, S.P.; Woinowsky-Krieger, S. *Theory of Plates and Shells*, 2nd ed.; McGraw-Hill: New York, NY, USA, 1959.
47. Ashby, M.F. *Materials Selection in Mechanical Design*, 4th ed.; Butterworth-Heinemann: Oxford, UK, 2011.

Disclaimer/Publisher's Note: The statements, opinions and data contained in all publications are solely those of the individual author(s) and contributor(s) and not of MDPI and/or the editor(s). MDPI and/or the editor(s) disclaim responsibility for any injury to people or property resulting from any ideas, methods, instructions or products referred to in the content.